


Review

# Optical Waveguide Refractive Index Sensor for Biochemical Sensing

Cheng Peng<sup>1,2</sup>, Changjin Yang<sup>1,3</sup>, Huan Zhao<sup>4</sup>, Lei Liang<sup>1,3,5,\*</sup> , Chuantao Zheng<sup>4</sup>, Chen Chen<sup>2,\*</sup>, Li Qin<sup>1,3,5</sup> and Hui Tang<sup>1,3</sup>

<sup>1</sup> State Key Laboratory of Luminescence and Applications, Changchun Institute of Optics, Fine Mechanics and Physics, Chinese Academy of Sciences, Changchun 130033, China

<sup>2</sup> School of Information Science and Engineering, Wuhan University of Science and Technology, Wuhan 430081, China

<sup>3</sup> Daheng College, University of Chinese Academy of Sciences, Beijing 100049, China

<sup>4</sup> State Key Laboratory on Integrated Optoelectronics, College of Electronic Science and Engineering, Jilin University, Changchun 130012, China

<sup>5</sup> Peng Cheng Laboratory, No. 2, Xingke 1st Street, Shenzhen 518000, China

\* Correspondence: liangl@ciomp.ac.cn (L.L.); chenchen@wust.edu.cn (C.C.)

**Abstract:** This study describes the basic principles of optical waveguide refractive index sensing and the various design structures of refractive index sensors. These waveguides generate different optical resonances, which cause changes in the sensing refractive index and temperature and are subsequently used to detect the concentration in the analyses. First, the structural characteristics and performance indices of the microring sensor and interferometer are studied based on the refractive index of the optical waveguide. Second, the principle and sensing detection mechanism of the two types of refractive index sensing employed in these sensors are analyzed. Then, the two sensors are classified and discussed from the perspective of the waveguide materials and structures, as well as the substances to be measured. Simultaneously, performance indicators such as sensitivity and detection range are compared and summarized. The comparison results show that there is a compromise between the sensitivity and quality factor of the optical waveguide refractive index sensor. Finally, applications of refractive index sensing in the biochemical field for material detection are discussed, showing that the optical waveguide refractive index sensor has significant advantages over other types of biochemical optical sensors.

**Keywords:** refractive index; optical waveguide; sensor; microring resonator; Mach–Zehnder interferometer



**Citation:** Peng, C.; Yang, C.; Zhao, H.; Liang, L.; Zheng, C.; Chen, C.; Qin, L.; Tang, H. Optical Waveguide Refractive Index Sensor for Biochemical Sensing. *Appl. Sci.* **2023**, *13*, 3829. <https://doi.org/10.3390/app13063829>

Academic Editor: Mario Lucido

Received: 2 February 2023

Revised: 10 March 2023

Accepted: 13 March 2023

Published: 16 March 2023



**Copyright:** © 2023 by the authors. Licensee MDPI, Basel, Switzerland. This article is an open access article distributed under the terms and conditions of the Creative Commons Attribution (CC BY) license (<https://creativecommons.org/licenses/by/4.0/>).

## 1. Introduction

With the rapid development of modern information technologies, such as the Internet of Things and big data, sensor technology, as the foundation of an intelligent information society and one of the three pillars of modern information technology, is currently receiving significant attention worldwide. High-sensitivity optical sensing technologies are applicable in industrial process control, national security, and other fields. With the development of optical integration technology, optical sensor devices have expanded from the study of optical fiber sensors to optical waveguide sensors that can be easily integrated [1]; in particular, we see an uptake in the use of optical waveguide technology for target detection in the fields of biology and chemistry.

Optical waveguides have advantages such as small size, simple structure, and easy integration, and they are sensitive to changes in the refractive index, absorption, and chemical processes. These changes modulate the light transmitted in the waveguide, and the properties of the optical waveguide can be used to fabricate various sensors [2]. Optical waveguide refractive index sensing uses optical phenomena, such as resonance and

interference, to detect the shift of the resonance peak or the attenuation of optical power according to the properties of different concentrations of target analytes. Compared with traditional sensors, optical waveguide refractive index sensors have advantages such as small size and low power consumption [3], and can rapidly, sensitively, label-free, and detect substances to be tested in a non-destructive manner. Hence, they have become a research field in the field of integrated optoelectronics in recent years.

Optical waveguide biochemical sensing is a combination of optical waveguide technology and biological and chemical technologies. Biosensors are a class of chemical sensors. Optical biochemical sensing can be divided into labeled optical biochemical sensing and unlabeled optical biochemical sensing (e.g., refractive index sensing) [4]. In the optical waveguide biochemical sensor, the evanescent field of the waveguide is altered by the changes in the refractive index, absorption coefficient, and other parameters, which is typically caused by the change in the phase of the transmitted light, resulting in a different effective refractive index of the optical transmission mode. The change in effective refractive index can be calculated by mode coupling theory, which is applied to sensors such as surface plasmon resonance (SPR) sensors and grating sensors. It can also be calculated based on phase changes, which is applied to devices such as microring resonators (MRRs), Mach–Zehnder interferometers (MZIs), multimode interferences (MMIs), fiber Bragg gratings, photonic crystals, and other differential interferometers [5,6]. Based on the refractive index change or absorption spectrum, optical waveguide refractive index biochemical sensors can be used for qualitative or quantitative analysis of gas, liquid, and solid substances to be tested [7]. Furthermore, they can be used for the detection of harmful gas concentrations in the environment, food and water quality monitoring, and bacteria and virus detection for public health issues and chemical threat perception [8]. The mechanism of biochemical sensors that use label-free detection is mainly based on the change of refractive index caused by molecular interaction to measure chemical substances, viruses, or bacteria, and it is related to the target sample concentration or surface density, which is easy to measure and low in cost. Sensing measurements are possible due to a change in the refractive index near the sensor surface due to the difference in refractive index between the target analyte and the buffer solution. In label-free optical sensors, the light is mainly concentrated on the sensor surface, and the evanescent field decays exponentially from tens to hundreds of nanometers in the target analyte, so it is possible to detect the change in the refractive index; however, for biomolecules that are not recognized and for analytes far from the sensing surface, the sensing signal is weak, so the target analyte can be distinguished from the buffer solution [9].

After conducting a literature review, it was found that Kozma et al. [10] conducted a review in 2014 that focused on biosensors based on integrated planar optical waveguide interferometer structures. They primarily analyzed and discussed the sensing structures of both common-path and double-path waveguide interferometers and compared the advantages and disadvantages of different methods and sensing structures. However, this review only focused on two types of waveguide interferometer sensing structures and lacked a detailed discussion on the sensing detection mechanism and performance, as well as application scenarios and the detection range. Therefore, further refinement and improvement of this study was necessary for a comprehensive understanding of the future development direction and achievements in this field.

In 2015, Patel et al. [11] conducted a review of sensors used to measure analytes related to food safety in fields such as chemistry and microbiology. However, the paper mainly focused on sensors that use microbial cells such as enzymes and immunoglobulin antibodies as biological components and did not comprehensively introduce and analyze sensors used in the biological and medical fields. Additionally, there was limited discussion on the principles and applications of new biomarker recognition components, and no detailed description of current research trends and future development directions based on biomarker recognition sensors.

In 2020, Wang et al. [12] reviewed the existing problems in optical waveguide biosensors at the field of food quality control. In view of the problems that silicon waveguides cannot transmit visible light and have poor corrosion resistance, they proposed to use diamond as waveguide core material, and listed the commonly used single structure and composite structure waveguide sensors. More recently, Butt et al. [13] reviewed the latest progress of sensors in environmental monitoring, mainly focusing on the detection of toxic gases, water quality, indoor environment, and natural disasters, without discussing molecular detection in other fields such as biomedicine, resulting in a limited application scope. In addition, there was a lack of introduction and classification of performance indicators such as sensor sensitivity and detection range, and there were few theoretical analyses. In addition, in 2022, Singh et al. [14] reviewed some of the marked advances in the last decade in the field of optical biosensors, including the classification, typical structure, and application of optical biosensors. As optical waveguide sensor is a subclass of optical sensor, the structure and application of optical waveguide sensor are briefly introduced in this paper, and the sensing mechanism is not discussed in depth.

It can be seen that the review of optical waveguide refractive index sensors in the above literature has its own focus, namely, as material, structure, application, etc. It is difficult to form a comprehensive understanding of such sensors through a single literature. Based on this, this article comprehensively reviews various waveguide refractive index sensors, introduces their applications in fields such as gas detection and biomedical engineering, and conducts detailed comparative analyses of the performance of different types of sensors, highlighting the factors that need to be considered in designing high-performance refractive index sensors. In chapter two, the structural principles, detection mechanisms, and performance indicators of MRR, MZI, and MMI structures of optical waveguide refractive index sensors are discussed. Chapter three provides a detailed introduction to refractive index sensors based on MRR, MZI, and MMI structures, comparing their performance in terms of sensitivity, detection limit, size, cost, and process complexity. Chapter four compares the performance and application range of optical waveguide refractive index sensors with other types of sensors. It also discusses the advantages and disadvantages of MRR, MZI, and MMI structure refractive index sensors under different materials. Chapter five analyzes the determining factors of sensor performance and application scenarios, pointing out that improving sensor performance requires by focusing on improving sensitivity, reducing loss, and expanding detection limits. In combination with recent research trends, it is suggested that micro and chip-scale sensors are the future development trend. Chapter six summarizes the entire article. Due to their high sensitivity, immunity to external electromagnetic interference, and miniaturization advantages, optical waveguide refractive index sensors are expected to be integrated on a chip in practical applications and are widely used in integrated optical devices. The research presented in this article is of great reference significance for the development of the sensor field.

## **2. Structural Principle, Detection Mechanism, and Performance Indicators**

### *2.1. Structural Principle of Optical Waveguide Refractive Index Sensing*

Refractive index sensing uses optical phenomena, such as light interference, diffraction, absorption, and dispersion, to demonstrate the different properties of different concentrations of target detection substances. When the detection substance flows through the sensor, it causes a shift in the resonant peak frequencies or a change in the optical power, leading to a change in the refractive index. The aim of detecting different components or substances with different concentrations can be achieved by detecting the change in the refractive index. At present, the common implementation methods for optical waveguide refractive index sensing are based on MRRs and MZIs. The structure and principles of these two optical waveguide refractive index sensors are described below.

### 2.1.1. Refractive Index Sensing Principle of a Microring Structure

Optical waveguide MRRs have good wavelength selection characteristics, high quality factor (Q), and compact structure, and their ring cavity can provide optical feedback. Therefore, they can be easily integrated with other optoelectronic devices and are widely used in integrated optoelectronics, optical communications, and other fields.

An MRR is generally composed of a microring waveguide and a strip waveguide. Light first enters the strip waveguide from the input end and then passes through the coupling area of the ring waveguide. The evanescent waves are excited by the light in the waveguide, some of them couple to the ring waveguide, while some couple to the strip waveguide in the near-field. The light coupled to the ring waveguide interferes with the light in the strip waveguide after traveling around the ring. In addition, the light waves that satisfy the resonant condition of the ring waveguide form a relatively strong optical field; that is, a resonance enhancement effect is generated, and the ring mode propagates circularly in the ring waveguide. Therefore, the guided wave optics theory and coupled mode theory form the theoretical basis of the MRR transmission principle [15]. The shapes of the MRR can be circular (Figure 1a), disk-shaped (Figure 1b), or racetrack-like.

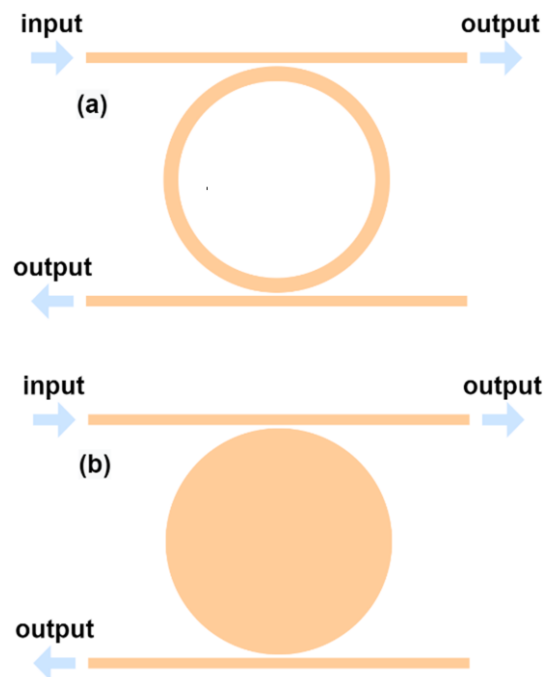


**Figure 1.** (a) Annular MRR; (b) disk MRR.

The theory of guided wave optics involves studying the transmission and electromagnetic field distribution of light in a waveguide. The function of the optical waveguide is to confine the light beam to the core layer and guide it to propagate along a certain direction. Because light is also an electromagnetic wave, the theory of electromagnetism based on Maxwell's equations applies to optical research. Furthermore, the Helmholtz equations were obtained using Maxwell's equations. Therefore, when analyzing the optical field in the optical waveguide, the specific electromagnetic field distribution can be obtained by solving the Helmholtz equations, as follows:

$$\begin{aligned}\nabla^2 \vec{E} + k^2 \vec{E} &= 0; \\ \nabla^2 \vec{H} + k^2 \vec{H} &= 0,\end{aligned}\quad (1)$$

where  $\nabla$  is Hamiltonian,  $k$  is wave number,  $\vec{E}$  is electromagnetic vector, and  $\vec{H}$  is magnetic field vector. The coupled-mode theory is derived from the transmission matrix theory,



which is a simplification of the guided-wave optics theory in specific cases and can rapidly solve the problems of certain types of waveguides [16]. The MRR structure can be considered as a coupler, and the general form of the coupled-mode equation is derived. Directional coupling can be used to exchange the optical power between the strip waveguides, and bending coupling can cause the light in the microring waveguide to resonate. An MRR can be designed using the resonance and filtering characteristics of the microring.

The principle of resonance in the microring is based on the interference of light. Light is input into the waveguide from one end and transmitted to the coupling area. Next, the light is coupled to the ring from the straight waveguide. When the wavelength of the light is an integer multiple of the length of the ring, resonances occur, yielding an output of light of the resonance wavelength at the other end. Incident light refers to a certain range of broad-spectrum light sources rather than specific wavelengths. In related research on MRRs, the microring resonance equation must be satisfied, as shown in Equation (2).

$$2\pi R n_{eff} = m\lambda, \quad (2)$$

where  $R$  is the resonance radius of the microring,  $n_{eff}$  is the effective refractive index,  $m$  is the resonance base and a positive integer, and  $\lambda$  is the resonance wavelength. The resonance base  $m$  is an important parameter because it is the mode order. Other parameters such as the resonance radius, radius-wavelength dispersion equation, free spectral region (FSR), and other expressions can be calculated for each resonance based on Equation (2).

### 2.1.2. Refractive Index Sensing Principle of MZI Structure

The interferometer structure can be divided into several types, such as the MZI, Fabry–Perot interferometer (FPI), and Young interferometer (YI). The MZI is the most commonly used and can be divided into symmetrical and asymmetrical MZI structure considering the symmetry of their two arms.

Furthermore, the MZI structure shown in Figure 2 includes an input waveguide, an output waveguide, a Y-shaped beam splitter, a Y-shaped coupler, and the sensing and reference arms located between the two Y-shaped junctions, which are constructed by a straight waveguide [17]. In the symmetric MZI, the laser is coupled to the input waveguide, which splits at the Y-junction to form two interferometer arms. The arms recombine at the next Y-junction to form the output waveguide, which then goes through the recombination at the Y-coupler. The sizes of the two arms are the same, and a sensing window with a bare core layer on the sensing arm is used to detect the object under test. It is worth noting that the reference arm is not in contact with the object under test; hence, the phase difference of the wave function in the two arms changes the output optical power. In addition, the characteristic parameters (such as the refractive index) of the material of the object under test on the sensing arm can be obtained. In the asymmetric MZI, the two arms are in contact with the object under test simultaneously; however, the two arm sizes are different; thus, the phase difference of the input light field during transmission causes a change in the output light power to provide a sensing detection.

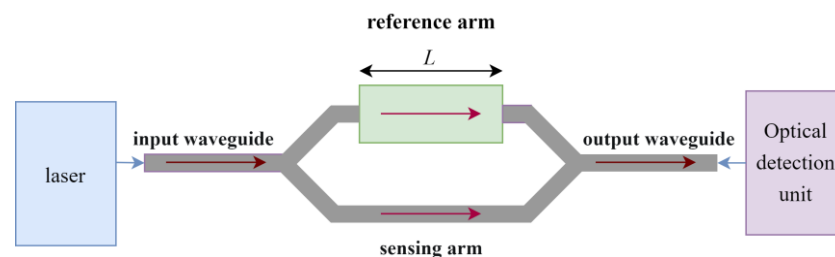


**Figure 2.** MZIs sensor structure diagram.

MZI sensors typically consist of a laser, light detection unit, sensing arm with an evanescent field sensing window, and reference arm. The light from the laser is coupled to

the input waveguide and divided into two similar beams at the beam splitter; these two beams travel a certain distance before re-combining at the coupler. Based on the theory of evanescent field sensing, the effective refractive index of the mode transmitted in the sensing arm is altered by the changes in its environment. As a result, phase modulation occurs through the interference of the two arms and generates a phase difference to enable detection. The phase difference  $\Delta\varphi$  can be expressed as follows:

$$\Delta\varphi = \frac{2\pi}{\lambda} \Delta n_{eff} L, \quad (3)$$

where  $L$  denotes the sensing window length of the sensing arm. The concentration of the substance under test can be determined by measuring the interference intensity at the output waveguide.

At present, several novel waveguide structures, such as slot, plasmonic, subwavelength grating slot, metal cladding, and composite waveguides, have been studied. These waveguides have improved the device sensitivity to a certain extent. However, they also increase the complexity of the waveguide design and difficulty of the device fabrication compared to conventional waveguides [18]. The materials used in the waveguide structures include silicon-based optical waveguide materials, chalcogenide compounds, lithium niobate compounds, and polymers [19].

### 2.1.3. Refractive Index Sensing Principle of MMI Structure

MMI utilizes the self-imaging principle of light to periodically replicate the input field profile at specific positions [20]. A typical MMI consists of three parts: input waveguides, a multimode waveguide region, and output waveguides. The width of the multimode waveguide region is wide enough to support multiple high-order waveguide modes. Using waveguide mode theory, the beat length of the two lowest-order modes is:

$$L_{\pi} = \frac{\pi}{\beta_0 - \beta_1} \approx \frac{4n_{eff}W^2}{3\lambda_0}, \quad (4)$$

where  $W$  approximates the width of the multimode waveguide region, and  $n_{eff}$  is the effective refractive index of the multimode interferometer region. Furthermore, it can be used to derive the expression for the propagation constant of the  $m$ th-order mode:

$$\beta_m = \beta_0 - \frac{m(m+2)\pi}{3L_{\pi}}. \quad (5)$$

When an input field profile  $\psi(x, 0)$  imposed the multimode waveguide region at  $z = 0$ , it is decomposed into the intrinsic modes of the multimode waveguide region:

$$\psi(x, 0) = \sum_m c_m \psi_m(x), \quad (6)$$

where  $c_m$  is the field excitation coefficients. When light propagates along the  $z$ -axis for a certain distance, the amplitude of each order mode remains unchanged, while the phase changes. Formula (6) can be expressed as:

$$\psi(x, z) = \sum_m c_m \psi_m(x) \times \exp\left(i \frac{m(m+2)\pi}{3L_{\pi}} z\right). \quad (7)$$

Although the accumulated phase of different-order modes is different, when phase matching condition are met, interference occurs among these modes, and the input field profile is reproduced periodically, which is called the self-imaging effect.

## 2.2. Refractive Index Sensing Mechanism

### 2.2.1. Microring Sensing Detection Mechanism

Optical waveguide biochemical sensors built with MRRs as basic components typically have two detection mechanisms to convert biochemical signals into optical signals. One is achieved by detecting the change in the resonant wavelength of the MRR, whereas the other is achieved by detecting the change in the output light intensity at a fixed single wavelength.

From Equation (2), it can be seen that a change in the effective refractive index causes a change in the resonant wavelength of the MRR. Furthermore, the effective refractive index of the transmission mode in the MRR is affected by the changes in the surrounding environment. During the sensing operation, the variation in the external environment can be measured based on the drift of the resonance wavelength and changes in the light intensity. Commonly used detection methods using MRRs for sensing are those based on the resonance wavelength shift and intensity variation.

The resonance wavelength drift method measures the measurement based on resonance wavelength drift  $\Delta\lambda$ . This sensing method has a wide measurement range. Figures 3 and 4a show the sensing implementation flowchart and detection principle of the resonance wavelength drift method, respectively. Moreover, the method based on the light intensity change measures the intensity change  $\Delta I$  at the resonance wavelength and detects the light intensity change in the output spectrum of the MRR. Figure 4b displays a schematic diagram of the intensity detection method, which can be represented by the resonance wavelength variation of the extinction ratio.

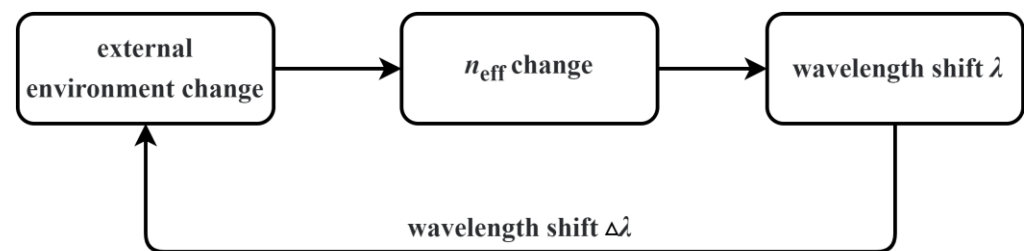


**Figure 3.** Sensing flowchart of resonance wavelength drift method.

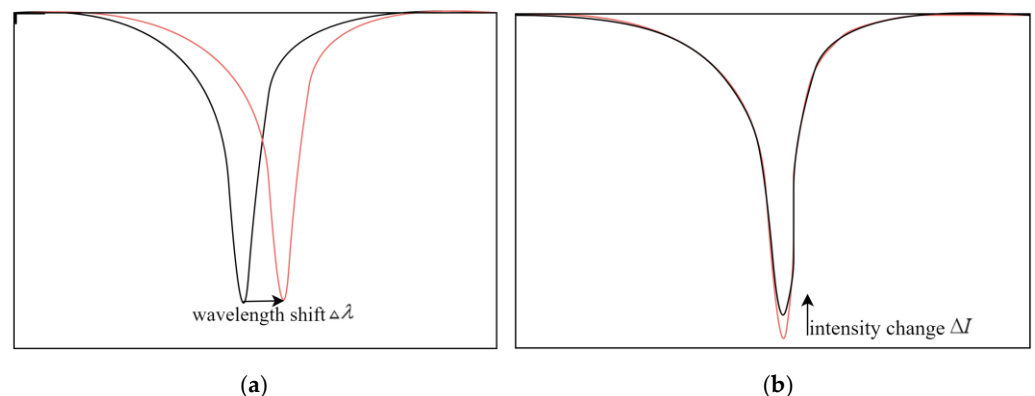


**Figure 4.** (a) Resonant wavelength shift method; (b) intensity variation method.

### 2.2.2. MZI Sensor Detection Mechanism

To derive the transfer functions of the input and output light intensity, the light beam splitter and coupler consisting of the two Y-shaped branch structures in the MZI refractive index sensor are divided into different sections, as shown in Figure 5.

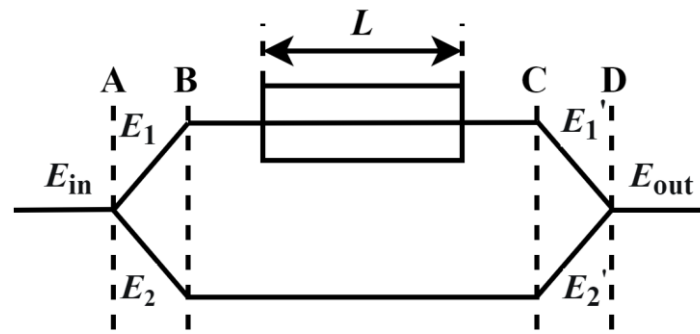


Figure 5. MZI refractive index sensing structural division.

Let  $E_m$  be the normalized mode field distribution ( $I_{in} = |E_{in}|^2 = 1$ ) of the waveguide; after the incident light passes through the first Y-branch structure, the light field is divided into  $E_1$  and  $E_2$  components. In addition, the field distribution in section B can be expressed as follows:

$$\begin{pmatrix} E_1 \\ E_2 \end{pmatrix} = \begin{pmatrix} a \\ b \end{pmatrix} \cdot E_{in}, \tag{8}$$

where  $a$  and  $b$  represent the amplitude distribution coefficients of the Y-branch beam splitter and satisfy the condition  $0 \leq a^2 + b^2 \leq 1$ . When  $a^2 + b^2 = 1$ , this is considered an ideal situation without transmission loss. When  $E_1$  and  $E_2$  pass through the sensing and reference arms of the MZI refractive index sensor, respectively, the field distribution in section C can be expressed as follows:

$$\begin{pmatrix} E'_1 \\ E'_2 \end{pmatrix} = \begin{pmatrix} \exp[i(\Delta\phi_m)] & 0 \\ 0 & 1 \end{pmatrix} \cdot \begin{pmatrix} E_1 \\ E_2 \end{pmatrix}; \tag{9}$$

$$\Delta\phi_m = \frac{2\pi}{\lambda} \cdot \Delta N \cdot L, \tag{10}$$

where  $\Delta\phi_m$  is the phase difference introduced by the object under test,  $\lambda$  is the wavelength of the incident light,  $L$  is the window length of the sensing arm of the sensor, and  $\Delta N$  is the difference in the refractive index between the sensing and reference arms. When the light components pass through the sensing arm and recombine at the Y-shaped branch, the field distribution in section D can be expressed as follows:

$$E_{out} = (a \ b) \begin{pmatrix} E'_1 \\ E'_2 \end{pmatrix} = (a \ b) \begin{pmatrix} \exp[i(\Delta\phi_m)] & 0 \\ 0 & 1 \end{pmatrix} \begin{pmatrix} a \\ b \end{pmatrix} E_{in}. \tag{11}$$

The relationship between the output and input light intensities of the MZI refractive index sensor can then be expressed based on Equation (8) as follows:

$$\frac{I_{out}}{I_{in}} = \left| \frac{E_{out}}{E_{in}} \right|^2 = a^4 + b^4 + 2a^2b^2\cos(\Delta\phi_m) = (a^4 + b^4) \left[ 1 + \frac{2a^2b^2}{a^4 + b^4}\cos(\Delta\phi_m) \right]. \tag{12}$$

Therefore, when  $a^2 + b^2 = 1$ , there is no loss in the Y branch, and the energy transfer coefficient is 1 in this case. Ideally, there is no loss in the Y branch; that is,  $(a^2 + b^2 = 1)$  is satisfied, and the transfer function between the output and input light intensities can be expressed as follows:

$$\frac{I_{out}}{I_{in}} = \frac{1}{2}[1 + \cos(\Delta\phi_m)]. \tag{13}$$

Generally, only the most ideal situation is considered; that is, the relationship between the output and input light intensities satisfies Equation (13).

Optical waveguide sensors mainly function based on the evanescent field principle. In an MZI sensor, the evanescent field changes via interaction with the external object under

test, resulting in a change in the refractive index. The refractive index change is converted into a measurable change in the output power or transmission spectrum. Therefore, to improve the sensitivity of the entire sensing device, the interaction strength between the evanescent field and external environment must be enhanced. This can be achieved mainly by changing the structure or material of the device.

### 2.2.3. MMI Sensing Detection Mechanism

Based on different incident conditions, MMIs can be classified into three types: (1) general interference, (2) paired interference, and (3) symmetric interference. The optical field simulation shown in Figure 6 is the simplest structure among the three types.

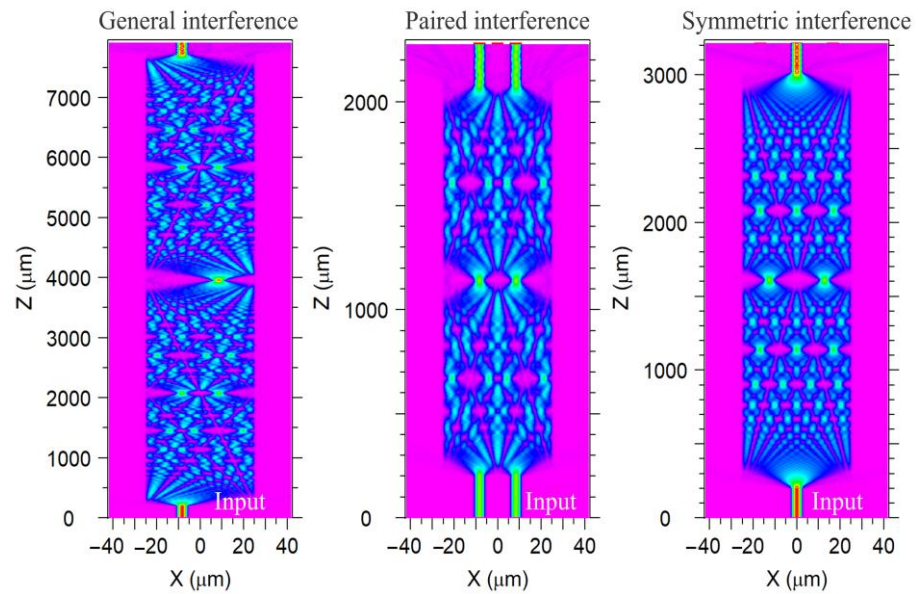


Figure 6. Three types of MMI structures.

When:

$$\exp\left(i\frac{m(m+2)\pi}{3L\pi}z\right) = 1 \text{ or } (-1)^m, \tag{14}$$

we can derive that when the length  $L$  of the multimode waveguide region satisfies the condition:

$$L = a \times 3L\pi (a = 0, 1, 2, \dots). \tag{15}$$

Images corresponding to the input field profile are formed at  $x$  and  $-x$ . Table 1 is the comparison of imaging characteristics. According to the above analysis, the detection mechanism of MMI is based on the fact that changes in the refractive index of the MMI medium affect the speed of light transmission and the phase shift in the waveguide. This, in turn, affects the interference phenomenon and causes changes in the intensity or wavelength of the output light. By measuring these changes, the variations in the refractive index of the surrounding medium can be determined.

Table 1. Comparison of imaging characteristics for the three types of MMI.

Interference Mechanism	General	Paired	Symmetric
Inputs × Outputs	$N \times N$	$2 \times N$	$1 \times N$
First single image distance	$3L\pi$	$L\pi$	$3L\pi/4$
First N-fold image distance	$3L\pi/N$	$L\pi/N$	$3L\pi/4N$
Excitation condition	none	$c_m = 0$	$c_m = 0$
		$m = 2, 5, 8$	$m = 2, 5, 8$
Inputs location	any	$y = \pm W/6$	$y = 0$

### 2.3. Performance Indicators for Refractive Index Sensing

Optical waveguide refractive index sensing is evaluated based on performance indicators, such as the free spectral range (*FSR*), quality factor (*Q*), wavelength full width at half maximum (*FWHM*), distinguish ratio (*DR*), sensitivity (*S*), and limit of detection (*LOD*) [21]. The sensitivity and detection limit are the two main criteria used for evaluating the performance of the optical biosensors, whereas the performance of waveguide optical biochemical sensors depends on the strength of the interaction between the solution or substance on the surface and light. The key performance indicators are as follows.

1. *FSR*: This parameter refers to the wavelength difference between two adjacent resonance peaks in the spectrum and can be expressed as follows:

$$\lambda_m = \frac{2\pi n_{eff} R}{m}; \quad (16)$$

$$FSR = \lambda_m - \lambda_{m-1}. \quad (17)$$

Let the group effective refractive index be  $n_g = n_{eff} - \lambda \frac{dn_{eff}}{d\lambda}$ , then Equation (17) becomes:

$$FSR = \frac{\lambda^2}{2\pi n_g R}. \quad (18)$$

It can be seen from Equation (10) that factors affecting the size of the *FSR* include the device radius *R*, light wavelength  $\lambda$ , and effective refractive index  $n_{eff}$  of the waveguide. In refractive index sensing applications, the *FSR* is an important performance indicator, which typically represents the detection range of the refractive index sensor.

2. *Q*: This parameter describes the sharpness of the resonant peak position in the spectrum of the MRR. The higher the *Q* value, the more sensitive the microring is to wavelength changes, and the better the performance of the sensor. It is expressed as follows:

$$Q = \frac{\lambda}{\Delta\lambda_{3dB}}. \quad (19)$$

3. *FWHM*: In the transmission spectrum of the microring, the full width at half maximum is the distance between two adjacent wavelengths when the power is reduced to half of the maximum power, which is also referred to as 3 dB bandwidth. This parameter determines the maximum data rate that can be processed and affects the detection lower limit of the sensor. *FWHM* can be determined using the following expression:

$$\Delta\lambda_{3dB} = \frac{\lambda^2}{2\pi R n_{eff}} \cdot \frac{1 - \alpha t^2}{t\sqrt{\alpha}}. \quad (20)$$

4. *DR*: This parameter is the resolution representing the minimum change that can be detected by the refractive index sensor. The output changes only if the change in the substance under test (such as the refractive index) is greater than the resolution. The resolution varies at each level within the sensing range of the sensor. This resolution can be expressed as three times the ratio between the system standard deviation  $\sigma$  and the sensitivity *S*:

$$DR = 3 \frac{\sigma}{S}. \quad (21)$$

5. *S*: Sensitivity and quality factors have an inverse relationship. In optical waveguide refractive index sensing, sensitivity can be expressed as follows:

$$S = \frac{\partial I_{out}}{\partial(n_m)} = \frac{\partial I_{out}}{\partial(\Delta\phi_m)} \frac{\partial(\Delta\phi_m)}{\partial(\Delta N)} \frac{\partial(\Delta N)}{\partial(n_m)}. \quad (22)$$

Each component in the formula can be further defined as follows:



- $\frac{\partial I_{out}}{\partial(\Delta\phi_m)} = -\frac{\alpha I_{in}}{2} V \sin(\Delta\phi_m + \Delta\phi_0)$ , the sensitivity function is a periodic function, and sensitivity changes periodically during testing;
  - $\frac{\partial(\Delta\phi_m)}{\partial(\Delta N)} = 2\pi \frac{L}{\lambda}$ , where  $L$  is the size of the sensing window; the larger the value of  $L$ , the more contact occurs between the sample under test and the sensing arm, the bigger the effective refractive index change of the guided mode, and the higher the sensitivity. Therefore, in terms of design requirements,  $L$  should be increased as much as possible to achieve improved sensing effects;
  - $\frac{\partial(\Delta N)}{\partial(n_m)}$  refers to the change in the effective refractive index of the guided mode on the sensing arm compared with the refractive index of the sample under test, which is primarily defined by the evanescent field strength dictated by the waveguide material and structure. This term can be increased by strengthening the evanescent field of the sensing waveguide.
6. *LOD*: this parameter is the minimum offset of the central wavelength of the resonance peak that can be detected by the detector. It is primarily related to the FWHM of the resonant peak, and half of the FWHM (HWHM) is typically taken as the offset of the central wavelength of the smallest resonant peak. *LOD* can be defined as the ratio of the smallest distinguishable wavelength drift to the detection sensitivity and is expressed as follows:

$$LOD = \frac{\delta\lambda_c}{S} = \frac{\delta\lambda_c}{\frac{\lambda_m}{n_{eff}} \frac{\partial n_{eff}}{\partial n_c}} = \frac{n_{eff}}{\frac{\lambda_m}{\delta\lambda_c} \frac{\partial n_{eff}}{\partial n_c}}. \quad (23)$$

Among them,  $\delta\lambda_c$  can be a part of the spectral width of the resonant peak. The spectral width is defined as the full width at half maximum FWHM of the resonant characteristic spectral line, and the relationship between it and the quality factor  $Q$  of the resonator is as follows:

$$\Delta\lambda_{FWHM} = \frac{\lambda_m}{Q}. \quad (24)$$

Thus, *LOD* can be expressed in terms of  $Q$  and  $S$  as follows:

$$LOD \sim \frac{1}{Q \cdot S}. \quad (25)$$

It can be concluded that the detection limit of the optical waveguide refractive index biochemical sensor is inversely proportional to its own  $Q$  and the detection  $S$  of the sensor. Therefore, to obtain a lower detection limit, sensor optimization can be achieved by improving the  $Q$  and  $S$  of the refractive index sensor.

### 3. Classification of Optical Waveguide Sensors

Integrated optical waveguides can be divided into passive devices (grating couplers, couplers, wavelength division/mode division multiplexers, filters, and isolators) and active devices (lasers, optical switches, modulators, and photodetectors). Passive device material systems include SiO<sub>2</sub>/SiN/SOI/SOS/chalcogenide glass (SOI is silicon on insulator and SOS is silicon on sapphire), whereas active device material systems include lithium niobate (LiNbO<sub>3</sub>)/polymer/germanium/gallium arsenide (GaAs)/indium phosphide (InP).

In terms of waveguide types, most devices are composed of strip and ridge waveguides. In addition, there are slot (slit), photonic crystal (PhC), subwavelength grating (groove), and surface plasmon trench waveguides. For the detection of biochemical substances in the form of gases or liquids, the concentration or density of the substance under test is the primary factor affecting the refractive index. The refractive index does not change with the volume of the substance under test; hence, it is suitable for the detection of trace substances. However, the refractive index change is not large; hence, it is necessary to improve the sensitivity of the sensor and expand the detection limit range.

### 3.1. Microring Structured Optical Waveguide Sensor

MRRs are a key component in the field of integrated optics and belong to the common refractive index sensor class, with several advantages such as a high quality factor, simple preparation, and easy mass production. Therefore, MRRs are widely used in the field of sensors, in addition to other fields such as lasers and detectors [22]. There are two approaches for improving the sensor LOD [23,24]. First, the quality factor  $Q$  of the resonator can be maximized to reduce the influence of noises on the measurement of the resonance wavelength. Second, the mean resonance wavelength shift can also be maximized by increasing the interaction between the light and biomolecules attached to the waveguide surface.

Materials used for integrated optics are increasingly diverse owing to the development of new materials such as  $\text{SiO}_2$ ,  $\text{LiNbO}_3$ , SOI, GaAs, InP, and organic polymers. SOI-based optical waveguide systems have several advantages such as a large refractive index difference, low transmission loss, and high integration capability.

#### 3.1.1. Silicon-Based Microring Optical Waveguide Sensor

In 2008, to realize the sensing and detection of weakly interacting gases, Robinson et al. [25] realized a slotted Si/ $\text{SiO}_2$  micron resonator. The enhanced effect of the slot waveguide on the optical field is combined with the refractive index sensitivity, and its scanning electron micrograph (SEM) images are shown in Figure 7. It combines the enhancement effect and refractive index sensitivity of the slit waveguide to the MRR. Furthermore, the relative refractive index of acetylene gas is detected under different pressures by measuring the change in the microring resonance wavelength. The slit width is 40 nm, resulting in a significant high electric field enhancement in the slit region. As a result, the refractive index (RI) sensitivity can reach 490 nm/RIU (refractive index unit), demonstrating that the light–liquid interaction is greater than that obtained using  $\text{Si}_3\text{N}_4/\text{SiO}_2$  groove waveguides. A resonator with a  $Q$  factor of 5000 was used to detect the refractive index change on the order of  $10^{-4}$ .

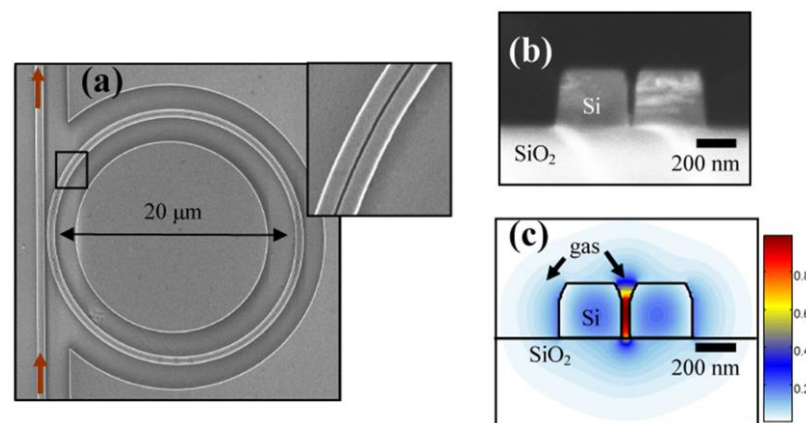


**Figure 7.** Scanning electron micrograph (SEM) image of silicon slit MRR. (a) Ring slot waveguide; (b) cross-sectional SEM image of the slot waveguide; (c) waveguide quasi-TE mode profile.

In 2007, Katrien et al. [23] proposed a label-free biosensor based on an SOI racetrack-shaped microring cavity. This biosensor can quantitatively measure trace substances and has the advantage of rapid preparation. The raceway shape has greater control over the coupling coefficient. Furthermore, the use of transverse waveguide coupling simplifies the fabrication process; SOI provides a high refractive index contrast, and the enhanced light field interacts with the substance under test in the cavity to increase the sensitivity and reduce the size of the sensor. It has an area of less than  $100 \mu\text{m}^2$ , a high  $Q$  factor, and a significantly small radius of  $5 \mu\text{m}$ . With a refractive index sensitivity of  $10^{-5}$ , owing to its small size, the device exhibits excellent sensitivity for absolute molecular mass sensing,

detecting protein concentrations as low as 10 ng/mL. In addition, it can be mass-produced and fully integrated on a chip, as shown in Figure 8.

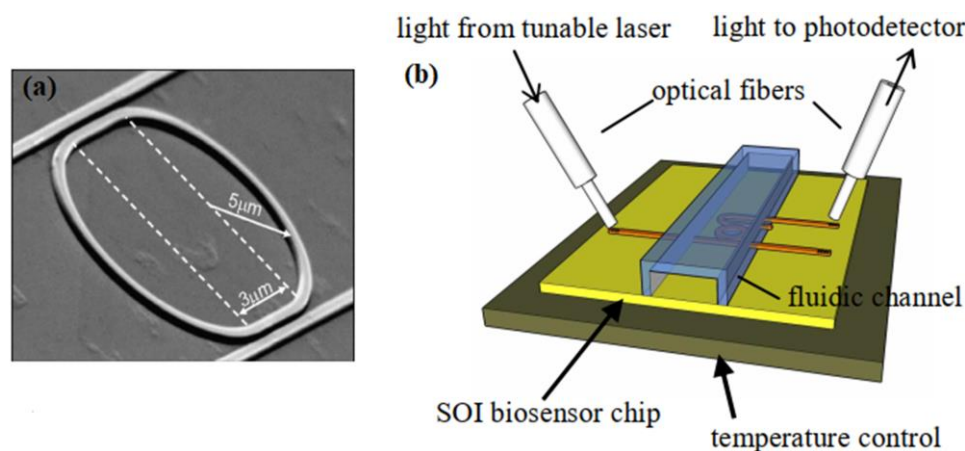


**Figure 8.** (a) SEM image of the microring cavity; (b) measurement device.

For the SOI platform, silicon is used as the layer material for the device; however, considering that silicon nitride has low refractive index and low temperature sensitivity and has a weak binding ability to light, sensitivity of silicon nitride devices can be improved. Therefore, in 2020, Liu Minghui [21] proposed a refractive index sensor based on a few-mode silicon nitride microring. This sensor detects liquid components by measuring the resonance wavelength shift by changing the refractive index of the object under test. The design parameters of the few-mode microring in the waveguide structure include a ring waveguide width of 2  $\mu\text{m}$  and a microring waveguide thickness of 0.4  $\mu\text{m}$ . The layer thickness of the silicon nitride wafer is 400 nm, whereas the wavelength and microring radius are 1550 nm and 30  $\mu\text{m}$ , respectively. The refractive index sensor can obtain a detection limit of  $10^{-5}$  RIU, sensitivity of 91 nm/RIU, and a Q value of  $2 \times 10^4$  or higher.

When a substance is attached to the ring waveguide, the effective refractive index ( $n_{\text{eff}}$ ) changes, thereby affecting the optical output power, which enables the measurements of the object under test. In 2014, Yang et al. proposed a microbiochemical sensor ring resonator based on an SOI planar optical waveguide [26]. The SOI optical waveguide adopts a ridge structure, the single-mode ridge waveguide is coupled with the ring waveguide to form a ring resonator, and its Q value can reach magnitudes of  $10^3$ . According to the optical waveguide theory, when the waveguide width is larger than 1  $\mu\text{m}$ , light is confined to the waveguide. This is not conducive to the coupling of the ring resonator. The width of the ridge waveguide used in this study is 0.45  $\mu\text{m}$ , while the wavelength is 1550 nm.

The detection limit of the sensor can be improved by maximizing the quality factor of the resonant cavity and increasing the interaction of light and biomolecules attached to the waveguide surface to maximize the average resonance wavelength shift per detection. In 2009, Claes et al. proposed a silicon-on-insulator ring resonator [27] based on slot waveguides. Compared with ordinary waveguides, slot waveguide resonators are used as biosensors in the fabrication of SOI rings. The sensitivity of the resonator is increased by a factor of 3.5 in detecting proteins. The area of the structure is 13  $\mu\text{m} \times 10 \mu\text{m}$ , whereas the sensitivity measured using a saline solution with a refractive index at a wavelength of 1550 nm is 298 nm/RIU, and the detection limit (the change in the refractive index of the top cladding) is  $4.2 \times 10^{-5}$  RIU. The ring resonator consists of a groove of width 104 nm and an SOI groove waveguide with a width of 268 nm. The device is fabricated using 193 nm optical lithography. The bending radius is set to 5  $\mu\text{m}$ .

In addition, in silicon-based microring optical waveguide refractive index sensing, the sensitivity is generally not high for the refractive index sensing of a single waveguide structure, such as a slot waveguide, slit waveguide, or one-dimensional photonic crystal microring. Therefore, researchers are now designing optical waveguide refractive index

sensors using composite structures, such as subwavelength grating and one-dimensional photonic crystal groove waveguide microrings.

In 2018, to solve the problems of low figure of merit (FOM) and low sensing performance of traditional microring sensors, Yujie proposed a one-dimensional photonic crystal slot waveguide microring refractive index using a high-quality factor sensor [28]. The sensing structure incorporates a ring-shaped photonic crystal slot waveguide into the traditional single-waveguide MRR. In addition, it confines the light field in the slot waveguide to the middle of the air hole and thereby improves the interaction between the light field and the substance under test. Optimizing the radius of the air hole on the microring slot waveguide resonator, the width of the slot waveguide, and the coupling distance between the resonator and waveguide can affect the sensing performance and improve the quality factor. The refractive index sensor consists of an annular photonic crystal slot waveguide, a quality factor that can exceed  $10^5$ , sensitivity of 97.47 nm/RIU, and an FOM value of  $6.63 \times 10^3$ . However, the structural model proposed in this study has only been simulated, and no actual sensor device was fabricated and tested.

In 2021, Dwivedi et al. proposed a method to obtain the dispersion turning point (DTP) in the dual-mode region by optimizing the core size of the metal-clad ridge waveguide (MUCRW). This approach enables ultra-high sensitivity in refractive index sensing of the nearby metal-clad ridge waveguide mode [29], as shown in Figure 9. The sensitivity of the refractive index sensing can reach 90  $\mu\text{m}/\text{RIU}$ , and the FOM value can reach 4500. The sensors considered in this study have great potential for biosensing applications owing to their ultrahigh volume and adhesion layer sensitivity.

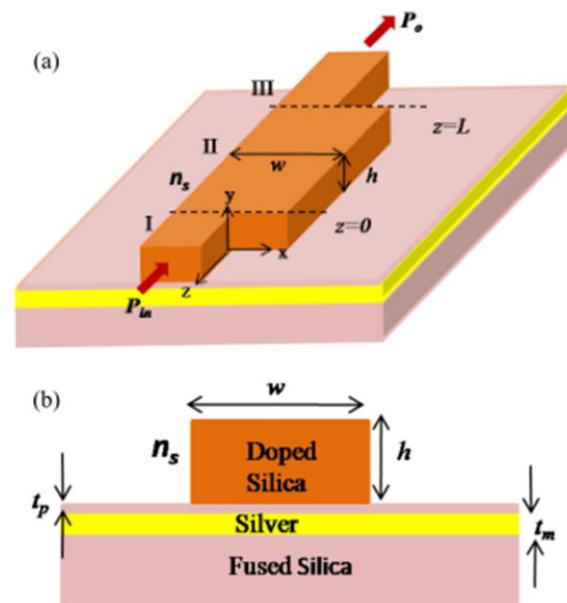


**Figure 9.** (a) Sensor structure; (b) cross-sectional schematic diagram of dual-mode waveguide.

Similar to the ridge waveguide, light is guided into the high-refractive-index material. However, the sensor also has shortcomings in biosensing applications. The interaction between light and the surrounding medium is significantly small, resulting in a small change in the index of the surrounding medium, which makes sensing and detection difficult. Therefore, Vivien et al. proposed a ring resonator based on vertical multi-slot silicon nitride waveguides [30]. In this study, a three-slot structure consisting of a silicon substrate, silicon oxide bottom cladding, a 300-nm thick silicon nitride layer, and silicon oxide top cladding was used. Compared with single-slit waveguides, the effective refractive index change of the  $\text{Si}_3\text{N}_4/\text{SiO}_2$  multi-slit structure-guided mode can be increased by 20% as a function of refractive index change in gas or liquid. The average FSR of the multi-groove ring resonator with a radius of 70  $\mu\text{m}$  was approximately 1275 nm. For a cavity

with a radius of 90  $\mu\text{m}$  and a gap of 400 nm, the  $Q$  factors of the transverse electric (TE) and transverse magnetic (TM) modes can reach 6100 and 16,000, respectively. The ring resonator losses were 28 dB/cm ( $R = 90 \mu\text{m}$ ) and 16 dB/cm ( $R = 110 \mu\text{m}$ ), respectively.

To improve sensitivity, a metal-assisted silicon slit waveguide structure was added to the traditional slit waveguide structure. By inserting a layer of Ag film, the optical confinement in the groove area can be enhanced and the evanescence rate of the optical mode can be improved, thereby improving the sensitivity of the sensor. In 2020, Zhang et al. proposed a novel on-chip gas sensor based on refractive index sensing to detect methane and carbon dioxide gases [31]. In their proposal, metal silver (Ag) was used in the sensor structure to design the slot waveguide, and  $\text{Si}_3\text{N}_4$  was used to replace the  $\text{SiO}_2$  material in the SOI. Because  $\text{Si}_3\text{N}_4$  has a lower transmission loss in the mid-infrared region than that of SOI materials, this wavelength range was selected for optical signals in the mid-infrared region. This design significantly improved the sensitivity of the refractive index sensing, and the range of evanescent waves could be extended to 0.48–0.85. The sensor structure enables real-time detection and exhibits good selectivity, making it a viable option for the design of future integrated photonic circuits. In addition, the sensing mechanism is suitable for a variety of active materials in the infrared range.

Using a multimode Fabry–Perot (FP) laser instead of a passive reference ring integrated in the system to generate the reference comb eliminates the requirement for an external broadband source and yields a higher spectral power density and energy efficiency. Compared with the transmission peak of the reference ring, the linewidth of the FP laser is narrower, thus increasing the sensitivity. In 2012, Song et al. proposed a high-sensitivity integrated optical biosensor based on the cascade of FP cavity lasers and MRRs [32]. Owing to the free spectral range of ring resonators and FP laser cavities, which is slightly different, the sensitivity can be significantly improved by using the Vernier effect, and a high sensitivity of 1000 dB/RIU can be achieved. The sensor structure comprises an FP cavity laser prepared on the InP base, an MRR designed on the SOI substrate, a 2  $\mu\text{m}$   $\text{SiO}_2$  insulating layer with a Si layer of 220 nm, and a 1- $\mu\text{m}$ -wide and 40-nm-high ridge waveguide structure. In addition, the diameter of the microring was 280  $\mu\text{m}$ , whereas the circumference was 885 nm; the waveguide was coated with an SU8 layer. When the ring resonator is exposed to the liquid to be measured, the change in the refractive index of the liquid sample causes a large shift in the envelope function of the total transmission spectrum of the sensor, resulting in a large change in the transmission power.

The FSR of the sensor limits the LOD, whereas increasing the circumference of the ring results in a smaller FSR, thereby improving the dispersion of the transmission characteristics. In 2017, Chandran et al. proposed SOI platform dispersion-enhanced critically coupled ring resonator refractive index sensing [33]. This type of sensing can be used for sensing a wide range of refractive indices (1.0–2.0) with a sensitivity of 380 nm/RIU. The sensor can measure the unknown refractive index of the analyte with a detection range of  $1.67 \times 10^{-2}$  RIU and a change in cladding refractive index of 0.5. Increasing the ring circumference can further reduce the detection limit to  $10^{-3}$  RIU without affecting the round-trip loss of the waveguide. The sensor device has a simple design, convenient operation, and a wide and accurate detection range.

Sensor sensitivity can be improved by changing the waveguide structure of the MRR. Luan et al. proposed a novel silicon photonic waveguide-based high-sensitivity sensor [34] by constructing an MRR which uses a silicon-on-insulator subwavelength waveguide consisting of five rows of periodic silicon square arrays with a pitch of 60 nm. The sensor achieved a higher bulk and surface sensitivity compared with that of other resonators using conventional strip waveguides. A bulk sensitivity of 579.5 nm/RIU and surface sensitivity of 1900 pm/nm can be obtained by exposing multiple MRRs to pure water and different concentrations of isopropanol solutions. Figure 10 shows a scanning electron microscopy (SEM) image of a 5-row multilayer MRR. The waveguide geometry is as follows: microring radius  $R = 30 \mu\text{m}$ , waveguide width  $w = 1200 \text{ nm}$ , waveguide thickness  $t = 220 \text{ nm}$ , grating period  $\Lambda = 240 \text{ nm}$ , and duty cycle  $\eta = 75\%$ . The  $Q$  of the 20  $\mu\text{m}$  microring was



significantly reduced ( $Q = 1700$ ) owing to high radiation loss. The FSR of the MRR was 6 nm, whereas the group index of the multilayer waveguide at 1550 nm wavelength was  $n_g = 2.15$ , and the bulk and surface LOD of the multilayer microring were  $1.02 \times 10^{-3}$  RIU and  $3.13 \times 10^{-1}$  nm, respectively. Compared with the recently reported subwavelength grating (SWG) MRRs, its bulk and surface sensitivities were improved by 1.5 times and 2 times, respectively. However, the  $Q$  value in water was low at 2600, which is lower than that of other SWG and silicon-based sensors.

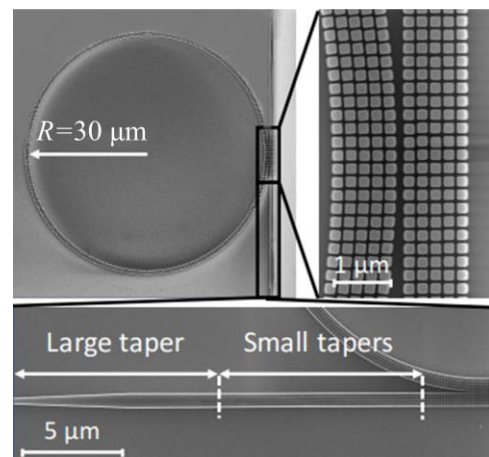


**Figure 10.** Scanning electron microscope (SEM) image of a 5-row multilayer MRR.

Future medical diagnostics will require biological detection using on-chip experimental techniques [35,36]. Silicon photonics enables the fabrication of compact planar sensors using integrated CMOS processes, making it a promising approach for large-scale on-chip biological detection. Zhang et al. [37] proposed a novel method for on-chip sensing using a silicon-based MRR and designed a refractive index biosensor based on a silicon slit waveguide ring resonator. By detecting the ring transmission spectrum, the shift of the envelope resulted in a quality factor peak range of 2000–6000 at the wavelength of approximately 1.5  $\mu\text{m}$ . Furthermore, by tracking the spectral envelope wavelength shift, the sensitivity  $S$  can reach 1300 nm/RIU when a liquid with a refractive index close to 1.33 fills the tank. The extinction ratio of the critically coupled resonance is greater than 20 dB, which implies that the LOD of the helically designed MRR in SOI photonics is lower than  $10^{-4}$ .

To achieve improved sensitivity and a lower detection limit of the biosensor, Huang et al. [38] proposed a silicon-based TM mode SWG waveguide MRR at a wavelength of 1550 nm. Owing to the enhanced interaction between photons and analytes, it exhibits improved sensitivity and a lower detection limit. When the coupling length is 6.5  $\mu\text{m}$ , the gap is 140 nm, and the silicon duty cycle is 0.7. The quality factor can reach a high value of 9800 in a water environment, and the bulk sensitivity was 429.7 nm/RIU. The corresponding detection limit was as low as  $3.71 \times 10^{-4}$  RIU, a reduction of 32.5% compared to the optimal value reported for other SWG microring sensors.

Compared with medium-refractive-index contrast material systems (such as  $\text{Si}_3\text{N}_4/\text{SiO}_2$ ), the use of high-refractive-index contrast material systems can reduce the size of photonic devices and increase the electric field strength at the slot waveguide interface, which improves the sensor sensitivity.

### 3.1.2. Chalcogenide Microring Optical Waveguide Sensor

Chalcogenide (ChG) rectangular waveguide sensors with small evanescent fields require a large waveguide length to enhance the light–gas interaction effect. To design a more compact sensor, Mingquan [39] proposed a mid-infrared chalcogenide (ChG)/silicon fluoride horizontal slot waveguide runway resonator sensor that detects methane ( $\text{CH}_4$ ). Optimization of the waveguide parameters was achieved through the use of a sulfide/silicon fluoride horizontal slot waveguide structure, as shown in Figure 11. A high-power con-



finement factor of 44.63% was obtained at a wavelength of 3291 nm, which is five times higher than that of other ChG rectangular waveguides. The waveguide length was reduced by at least 30 times by optimizing the sulfide/silicon fluoride horizontal groove waveguide. The resonator has an *LOD* of 3.87 ppm, an intrinsic waveguide loss of 3 dB/cm, an amplitude-coupling ratio of 0.1, and a response time of less than 5  $\mu$ s.

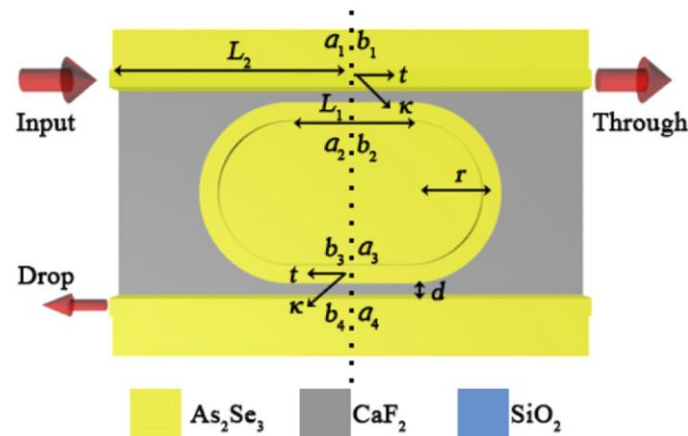


**Figure 11.** Horizontal slot waveguide runway resonator sensor top view.

Chalcogenide materials exhibit excellent application prospects in the mid-infrared wavelength range and near-infrared wavelength range. Compared with other materials such as silicon,  $\text{Si}_3\text{N}_4$ , or polymers, the medium refractive index (RI) of the  $\text{Ge}_{28}\text{Sb}_{12}\text{Se}_{60}$  chalcogenide material enables the optical field to maintain a strong confinement at small bending radii while achieving a high sensitivity and high *Q*. Huang et al. [40] proposed a liquid refractive index sensor using a Ge-Sb-Se MRR at a wavelength of 1550 nm to detect different concentrations of NaCl solutions. The chalcogenide glass material  $\text{Ge}_{28}\text{Sb}_{12}\text{Se}_{60}$  enables the obtainment of a high sensitivity of 123 nm/RIU and high quality factor of  $7.74 \times 10^4$ . The transmission loss of the waveguide is 4.3 dB/cm, extinction ratio is approximately 40 dB, and *LOD* is approximately  $3.24 \times 10^{-4}$  RIU. Owing to the high refractive index contrast between the ChG core and  $\text{SiO}_2$  substrate, the device size can be reduced to the order of tens of micrometers without adding substantial bending losses.

ChG groove (ChGS) MRRs have broad application prospects in the field of mid-infrared high-sensitivity sensing. Zhang et al. [41] fabricated a highly sensitive sulfide slit MRR and proposed a ChGS MRR using GeSbSe thin film as the groove. The power confinement factor (PCF) was enhanced through optimization of the core layer in the MRR. Compared to the traditional evanescent-field waveguide sensor, the proposed structure optimizes the curved groove waveguide to improve the sensitivity of the sensor. By fitting the resonance peaks with a Lorentzian curve, the cavity realizes a quality factor of  $1 \times 10^4$ , which is one of the highest quality factors reported thus far for chalcogenide groove MRRs. The sensor has a sensitivity of 471 nm/RIU, which results in a detection limit of  $3.3 \times 10^{-4}$  RIU.

In ring-resonator sensors, the shift of the resonant wavelength is typically used to study the sensing phenomenon. Ashok et al. [42] proposed a GeAsSe sulfide slit-ring resonator for refractive index sensing. The sensitivity can reach 42 nm/RIU with the highest FWHM value of 0.7 nm and a *Q* value of  $6.5 \times 10^3$ . When the refractive index was varied from 1.33 to 1.43, the sensitivity of the structure was 42 nm/RIU at a wavelength of 1551.03 nm. When the effective index difference was set to 0.005, the minimum *LOD* of the slot MRR was  $10^{-3}$  RIU. The refractive index sensor was fabricated using photolithography and inductively coupled plasma (ICP) etching to deposit chalcogenide glass on a silicon oxide wafer.

Chalcogenide glass has been identified as the material of choice for the design of highly specific and sensitive integrated sensors, because of their wide infrared transparent

windows. Richardson et al. [43] proposed a compact microdisk resonator to achieve a new type of high-refractive-index contrast. The sensing material used in this study, chalcogenide glass, also has potential applications in biochemical sensing. The sensor has single-mode waveguide capability with core dimensions down to the submicron range. Through testing, the refractive index sensitivity was determined to be 182 nm/RIU. Based on the water absorption coefficient of  $\alpha = 9.6 \text{ cm}^{-1}$  at a wavelength of 1550 nm, the estimated absorption limiting factor  $Q$  was 19,000.

Wang et al. [44] proposed a nonlinear refractive index sensor based on a coupled waveguide MRR, which consists of a coupled circular resonator with radius  $R$ . The sensitivity of the nonlinear microresonator refractive index sensor proposed in this study compared to the RI changes was two orders of magnitude higher than the theoretical sensitivity value of the linear microresonator RI sensor, and the  $LOD$  of chalcogenide glass reached  $10^{-12}$  RIU for Si.

### 3.1.3. Lithium Niobate Compound Microring Optical Waveguide Sensor

At present, optical waveguide sensors fabricated from lithium niobate materials are used for electric field measurement. In addition, they are used in various high-performance and high-power photonic microdevices, including high- $Q$  WGM resonators [45,46], photonic crystal (PhC) cavities [47], hybrid lithium niobate on insulators (LNOI) platform [48–50], and microwave photonics [51–56]. Currently, their use in biochemical sensors is relatively small. In addition, optical MRRs based on SOI technology have the advantages of strong optical confinement, small transmission losses, small bending radius, and a well-established manufacturing process. The high refractive index contrast of LNOI can result in a higher mode confinement and a lower bending radius, which enables the fabrication of small devices in integrated optics. Moreover, biosensing with a large measurement range requires ultra-high sensitivity and low detection limits, and research in this area is still ongoing [57].

Guarino et al. demonstrated a ring microresonator with a  $Q$  factor of only  $4.0 \times 10^3$  [58], whereas Hu et al. demonstrated an optical ridge waveguide with an optical loss of 6.3 dB/cm [59]. The highest  $Q$  factor of the LNOI microdisk resonator [60] reached  $4.7 \times 10^7$ , whereas the lowest optical loss in single- and multimode LNOI waveguides was 0.029 dB/cm [61] and 0.027 dB/cm [62,63]. The  $Q$ -factor and optical loss in the LNOI photonic structure improved by approximately four orders of magnitude.

Naznin et al. [64] designed and simulated a label-free optical MRR biosensor based on LNOI technology. To obtain a high sensitivity and large measurement range, the sensor uses a double MRR model and transmission spectrum obtained from 2D simulation based on the finite-difference time domain method. The refractive index of the sensing layer was between 1 and 1.45, and the LNOI consisted of an outer and inner ring of 10  $\mu\text{m}$  and 5  $\mu\text{m}$ , respectively. The sensitivity of the microring sensor is close to 68 nm/RIU, whereas the minimum  $LOD$  is  $10^{-2}$  RIU. The performance of the sensor was simulated with a glucose solution model.

With the development of technology, both fluidic channels and waveguides can be laser-written in glass, thereby paving the way for 3D optofluidic chips. Because a self-trapped beam can be formed in a monolithic lithium niobate chip structure, an optical waveguide refractive index sensor on a lithium niobate substrate can be fabricated using this technology. Chauvet et al. [65] proposed a refractive index sensor, in which a ring-shaped optical waveguide embedded in a lithium niobate substrate passes through a fluid channel, enabling accurate measurement of the refractive index of transparent liquids. A sensor was used to detect the refractive index of methanol, and the measured refractive index at 640 nm was 1.317. When the refractive index was between 1 and 1.8, the sensitivity of the sensor was approximately  $5 \times 10^{-3}$ .

Owing to the advantages of silicon waveguides such as low loss and low cost, most integrated optical sensing devices use silicon nitride/silicon dioxide technology [36]. However, a disadvantage of the technology is the inability to externally control the light, which is necessary in defining the operating point of an interferometric device. Moreover, lithium

niobate has the advantage of controlling light via the electro–optic effect and can be used to obtain waveguides with low losses and high resistance to light damage. To develop LiNbO<sub>3</sub> biochemical optical waveguide sensors, the binding process of the antibodies on the waveguide should first be studied. Suarez et al. [66] developed an LiNbO<sub>3</sub> biochemical optical waveguide sensor consisting of a planar waveguide fabricated on LiNbO<sub>3</sub> using the gas-phase Zn diffusion method and a low-loss optical waveguide. LiNbO<sub>3</sub>:Zn is a material with potential advantages in protein detection technology owing to its electro–optic properties. To develop biochemical sensors using LiNbO<sub>3</sub> waveguides, the binding problem of biomolecules to waveguides prepared via Zn diffusion must be solved first. The calculations yielded a detection limit of around 700 molecules per pixel. The results show that the light attenuation through the LiNbO<sub>3</sub> waveguide can detect surface-attached proteins via emission or absorption measurements. The combination of antibodies and waveguides facilitates the use of antigen–antibody interactions as a model, which paves the way for biosensor design based on LiNbO<sub>3</sub>:Zn waveguides.

### 3.1.4. Polymer-Based Microring Optical Waveguide Sensor

In recent years, integrated optical waveguide sensors have exhibited many advantages, such as being label-free, highly sensitive, and capable of real-time detection, in addition to having excellent potential in biochemical sensing and monitoring [67]. Traditional sensing is based on the evanescent wave principle, and the light–matter interaction in the cladding part is relatively weak. Moreover, the slit waveguide structure increases the interaction between the light and low refractive index, which improves the sensing sensitivity. In addition, research on slit waveguides has primarily focused on SOI materials. Polymer-based optical waveguides have the advantages of speed, high efficiency, and low cost. Huanlin et al. proposed a polymer-based slit waveguide microring refractive index sensor [68]. First, a silicon master mold was prepared, and a flexible soft mold was prepared using the fluorinated polymer perfluoropolyether (PFPE) on the silicon master mold. A polymer-based slot waveguide was fabricated using a UV soft imprinting process. The polymer slit waveguide microring structure is shown in Figure 12, and the width and height of the waveguide and the width of the slit waveguide were approximately 510, 830, and 234 nm, respectively. The working wavelength was the near-infrared band at 890 nm, and the sensitivity was 130 nm/RIU.

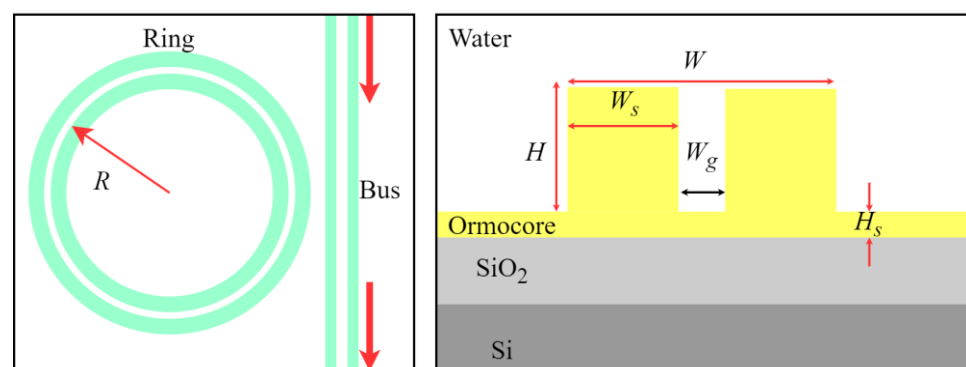


**Figure 12.** Polymer-based slit waveguide microring.

Ring optical resonators in single-mode waveguides can improve the sensitivity of devices owing to their low modal dispersion, low propagation loss, and small size. To further realize low-cost and large-scale production, multimode waveguide resonators with linewidths of several micrometers must be designed for refractive index sensing. However, it is difficult to use the resonator as a sensor because of the multiple peaks in the output transmission spectrum owing to modal dispersion. The S-bend resonator can eliminate the multi-peak problem using mode-recognition technology. Kim et al. proposed a polymer S-bend optical resonant cavity structure composed of multimode waveguides

for refractive index sensing [69]. Optical resonator sensors detect changes in the external effective refractive index by measuring changes in the resonance wavelength peak caused by changes such as antigen–antibody reactions, temperature changes, and protein binding in the sensing region. Figure 13 shows a schematic of an S-shaped curved resonator, where  $N$  is the number of curved waveguide layers and  $R$  is the radius of the curved waveguide. The performance of the S-bend resonator is related to the waveguide slope owing to the thermal reflow of the low-viscosity SU8 polymer. It was found that reducing the sidewall angle can increase the range and intensity of the evanescent field, resulting in an enhanced resonator sensitivity owing to the change in the external refractive index. This study provides a possibility for polymer-based millimeter-wave optical waveguide refractive index sensors.

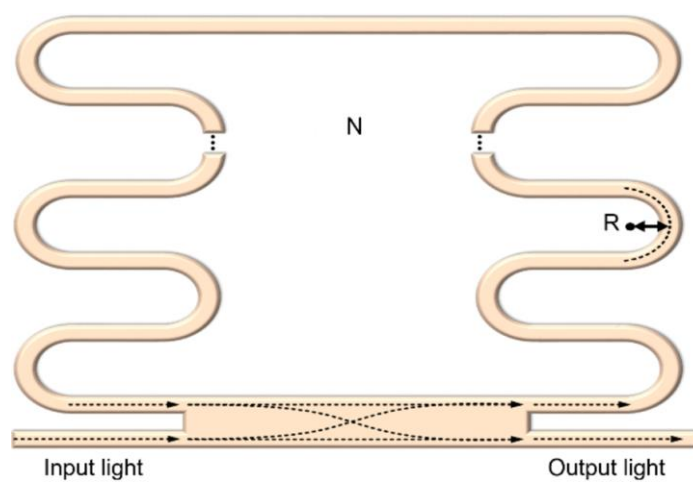


**Figure 13.** Schematic diagram of an S-shaped bending resonator.

Finally, the performance of the microring-based optical waveguide refractive index sensor was compared with that of previously reported sensors, and a summary is shown in Table 2. In addition, the performance of the microring optical waveguide refractive index biochemical sensor with different materials and structures was compared.

**Table 2.** Performance comparison of microring structure optical waveguide sensors.

Year	Unit	Construction	$S$ (nm/RIU)	$LOD$ (RIU)	$Q$
2008	Cornell University [25]	Silicon slot MRRs	490		5000
2009	University of Ghent, Belgium [27]	Slot waveguide SOI (silicon on insulator) ring resonator	298		
2018	Beijing University of Posts and Telecommunications [28]	One-dimensional photonic crystal slot waveguide microring	97.47		$10^5$
2020	Shanghai Jiaotong University [16]	Few-mode SiN waveguide ring sensor	91.79	$10^{-5}$	$2 \times 10^4$
2017	University of Southern California [31]	SOI coupled-ring resonators	382	$10^{-3}$	
2012	Zhejiang University [32]	Sensors based on cascaded FP cavity lasers and MRRs	1000		$3.8 \times 10^6$
2016	University of Paris-Saclay [37]	Silicon slot waveguide ring resonator	1300	$10^{-4}$	
2019	Columbia University [34]	Silicon photonic waveguide sensors	579.5		1700
2012	University of Central Florida [43]	chalcogenide glass compact microdisk resonance	182		19,000
2021	Ningbo University [40]	Ge-Sb-Se MRR	123	$10^{-4}$	$7.7 \times 10^4$
2022	Ningbo University [41]	ChGS slot MRR	471	$10^{-4}$	$1 \times 10^4$
2016	Khulna university [64]	LNOI label-free optical MRR	68	$10^{-2}$	
2020	Dalian University of Technology [68]	Polymer-based slot waveguide microring	130		

### 3.2. MZI-Structured Optical Waveguide Sensor

MZI-structured sensors are common label-free optical sensing devices. Their structure is relatively simple, easy to integrate, and can be used with special materials or combined with other flexible optical devices. The detection limit is generally between  $10^5$  RIU and  $10^7$  RIU. It has the advantages of high refractive index sensitivity, strong anti-interference ability, and high detection efficiency and exhibits good research significance and application value in biochemical sensing.

Optical waveguide sensors, such as optical waveguide temperature sensors, stress sensors, and various optical waveguide biochemical sensors, are research hotspots worldwide. Research on optical waveguide biochemical sensors has primarily focused on surface plasmon resonance and waveguide grating sensors. These sensors exhibit high sensitivity and response recovery characteristics. However, selectivity is poor, and the anti-interference ability is weak. The MZI optical waveguide sensor has the advantages of high sensitivity, strong selectivity, anti-interference ability, and small size. According to previous reports, the phase-difference resolution of the MZI optical waveguide sensor can reach  $5 \times 10^{-5} \times 2\pi$ , and the resolution of the refractive index change is approximately  $2 \times 10^{-8}$ . The detection of the lowest concentration of specific analytes was  $10^{-6}$ . The transmission loss of the optical waveguide is required to be less than 1 dB.

MRRs and MZIs are two common configurations used in waveguide-based sensors for optical signal readout. MRR biochemical sensors exhibit high sensitivity during the detection of proteins, DNA, viruses, and bacteria [9]. Wavelength-tunable lasers and spectral analyzers are required to perform wavelength scanning, and the detection limit of MRR-based sensors is limited by the resolution of expensive and complex external devices. By contrast, the MZI readout configuration is based on the detection of light intensity and does not require tunable lasers or optical spectrum analyzers. Therefore, miniaturization and integration of an optical waveguide MZI as a sensing platform system is feasible.

#### 3.2.1. Silicon-Based MZI Optical Waveguide Sensor

The MZI optical waveguide sensor has the advantages of high sensitivity, small size, and strong anti-interference ability, and has attracted increasing attention in the field of biochemical sensing [70,71]. In the literature, the refractive index of the MZI optical waveguide sensor is approximately  $2 \times 10^{-8}$ , and the lowest concentration detection value can reach  $10^{-6}$  [35].

Moreover, CMOS circuits based on SOI materials have the advantages of low power consumption, high integration density, strong anti-interference ability, and improved performance compared to those of traditional silicon-integrated circuits. With advantages of miniaturization, integration, and high sensitivity, new applications of biochemical sensors can be realized. Yang et al., from Tsinghua University, proposed a biochemical sensor based on an SOI planar optical waveguide [72]. The micron-sized sensor chip used CMOS technology. The sensitivity of the sensor can reach magnitudes of  $10^{-7}$  and the corresponding changes of the output optical power in the order of  $10^{-3}$  magnitude.

A conventional MZI sensor consists of two channels: a beam splitter and a coupler connected by a sensing arm and reference arm. To prevent evanescent coupling between the waveguides, the arms must be relatively wide apart, and to recombine the signals through the channels, additional bending or coupling structures are required, all of which increase the size of the device. To reduce the size of the sensing area, a single-mode helical waveguide is used in a conventional dual-channel MZI; however, balanced helical arms and additional structures are still required for splitting and combining light. Liu et al. [73] proposed a compact single-channel MZI biochemical sensor that consisted of two single-mode silicon waveguides and used dual transverse mode helical waveguides for sensing. The discontinuous node output is shown in Figure 14. Different concentrations of NaCl solutions were injected into the sensor to measure the bulk refractive index sensitivity of the sensor, which was  $461.6 \pi/\text{RIU}$ . The surface sensitivity of the sensor was found to be  $1.135 \pi/\text{ng mm}^{-2}$ . By sampling the optical response of the stable region, the sen-



sor exhibited a resolution of  $0.01 \pi$  and a detection limit of  $2.2 \times 10^{-5}$  RIU. Finally, the biosensing ability of the sensor was verified by measuring biotin–streptavidin interactions at different concentrations.

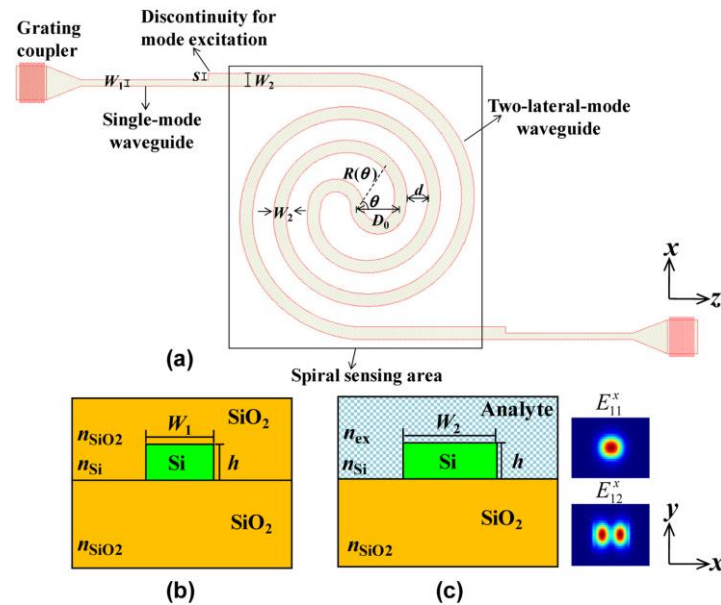


**Figure 14.** (a) Schematic diagram of the proposed sensor; (b) cross-section of a single-mode waveguide; (c) cross-section of a dual-mode waveguide and the electric field intensity distribution of the two transverse modes.

To improve the sensitivity and detection limit of the sensor, this study utilized the high sensitivity of the MZI and the architectural improvement introduced by the Vernier effect. In 2013, La Notte et al. [74] proposed an ultra-high-sensitivity chemical optical waveguide sensor using the MZI-enhanced Vernier effect, and the sensor chip was fabricated from compact SOI material. A CO<sub>2</sub> sensor was designed, capable of detecting gas concentrations as low as 5000 ppm, with significantly low detection limits, less than  $5.5 \times 10^{-7}$  RIU, and a sensitivity greater than 1000  $\mu\text{m}/\text{RIU}$ . In addition, an ultra-high-sensitivity MZI-enhanced Vernier effect NH<sub>3</sub> sensor for aqueous solutions was designed. The sensor can detect ammonia concentrations as low as 2 ppm, with a sensitivity as high as 2500  $\mu\text{m}/\text{RIU}$ , and an ultra-low LOD of  $8.79 \times 10^{-8}$  RIU.

For the MZI sensing platform to be easily integrated with optical fiber communication systems and optoelectronic systems, the coupling efficiency of the large-section SOI ridge waveguide and the standard single-mode glass fiber must be high. Furthermore, the matching must be improved, and the size of the MZI branch must be small. The sensing platform is compact and can achieve a micron level. According to the analysis, the trench-based MZI structure exhibits an improved performance compared to conventional configurations. Therefore, using the basic EH polarization mode (hybrid mode in which the electric and magnetic field components are mixed together, defined as EH mode) of the SOI ridge waveguide, Yuan et al. [75] proposed an MZI biochemical sensor based on a large-cross-section SOI ridge waveguide, as shown in Figure 15. At a working wavelength of 1550 nm, a uniform sensitivity of 7296.6 %/RIU was obtained. Its LOD can reach  $2.74 \times 10^{-6}$  RIU, which is lower than that of the refractive index of the Si<sub>3</sub>N<sub>4</sub> ridge waveguide (less than  $7 \times 10^{-6}$  RIU).



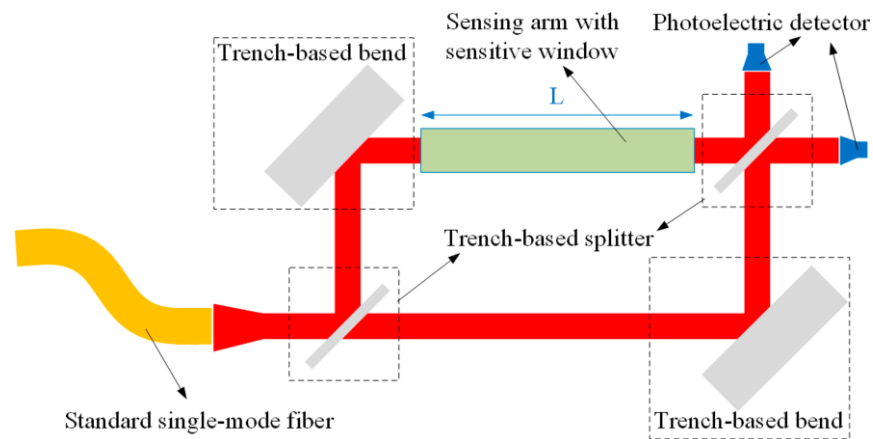


**Figure 15.** Schematic diagram of the MZI sensing platform based on a large-section silicon-on-insulator (SOI) rib waveguide.

Xie et al. [76] proposed a sensor design rule based on MZI, as shown in Figure 16. By properly selecting the MZI arm length, sensitivity can be adjusted to a value that is higher than that of any other traditional MZI sensors. Using SOI materials, a low-cost optical sensing system can be realized via proper selection of MZI arms with a device sensitivity as high as  $10^6$  nm/RIU and a detection limit as high as  $10^{-6}$  RIU.

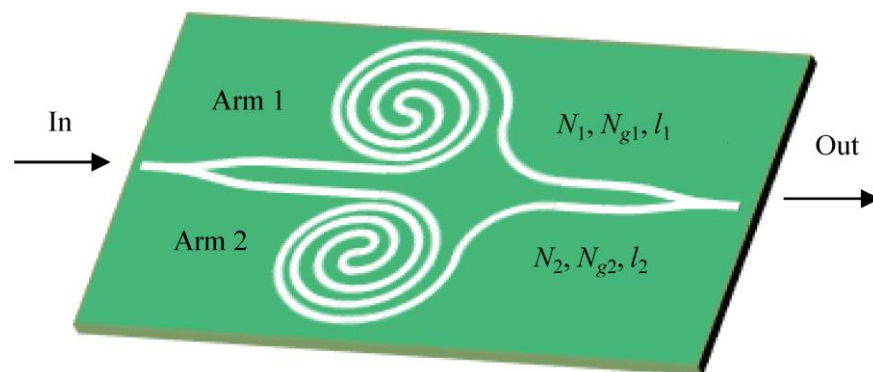


**Figure 16.** MZI sensor.

Conventional MZI sensors that use intensity interrogation require highly sensitive power sensors and highly stable systems to achieve low noise levels and high sensitivity. Although sensors with ring-resonator structures can overcome this problem by determining the wavelength shift with high precision, a high-resolution spectrometer is required. For the reported sensors based on two cascaded ring resonators, the Vernier effect was used to significantly improve the sensitivity. However, the extremely high sensitivity resulting from a significantly large Vernier factor has some disadvantages. Jiang et al. [77] realized ultra-high-sensitivity silicon photonic biosensors using cascaded MZIs and ring resonators with the Vernier effect. The sensitivities of the MZI and MZI ring sensors obtained were as high as 2870 and 21,500 nm/RIU, respectively. Biosensing applications were demonstrated by monitoring the interaction between goat and anti-goat immunoglobulin G (IgG). The measurement results showed that 1 ng/mL IgG resulted in a wavelength shift of 0.035 and 0.5 nm for the MZI and MZI ring sensors, respectively. For the MZI and MZI ring-based sensors, the measured temperature drifts were 76 and 271 pm/°C, respectively, and highly sensitive sensors are anticipated to be used in medical diagnosis.

Exposure to pyridine vapor can inhibit the nervous system, leading to poisoning. Therefore, there is an urgent need to develop a safe and reliable sensing technology to monitor its concentration in real-time. Zhao et al. [78] proposed an MZI microsensor based on a CMOS-compatible silicon nitride ( $\text{Si}_3\text{N}_4$ ) waveguide with bipolar polycarbonate as

the sensitive cladding material. The waveguide width and cladding thickness were varied to tune the group index and evanescent field. In the final experiment, the sensitivity of pyridine vapor can reach 63 pm/ppm, LOD was as low as 476 ppb, and the response time was significantly reduced. The designed MZI sensor exhibited ultra-high sensitivity, and the refractive index sensing sensitivity was greater than 30,000 nm/RIU in both the TE and TM modes.

### 3.2.2. Chalcogenide MZI Optical Waveguide Sensor

Biochemical sensors have significant research significance in the field of photonics. The increasing number of compounds has led to an increasing demand for monitoring systems with high sensitivity, wide detection range, high stability, and low response time [79,80]. The on-chip integration of photonic sensors operating at near-infrared wavelengths has been reported [81], and miniaturization can also be considered in mid-infrared sensing. Recent advances have enabled the combination of mid-infrared (MIR) light sources (such as quantum cascade lasers), waveguides, sensors, and detectors on the same chip [82–84]. There is a large selection of waveguide materials available. Among them, chalcogenide thin films are suitable for several MIR photonic applications in sensing [85–90]. Chalcogenide materials are particularly suitable for chemical sensing because most molecules vibrate in the infrared medium.

Baillieul et al. [91] developed a Ge-Sb-Se microsensor device for in situ monitoring of pollutants in environmental water, as shown in Figure 17. The sensor detects pollutants in natural water in the mid-infrared spectral range of organic compounds. The experimentally obtained detection of monoaromatics (BTX) using polyisobutylene (PIB) facilitates the development of chalcogenide film-based optical microsensors with sensitivities ranging from tens of ppb to hundreds of ppm.

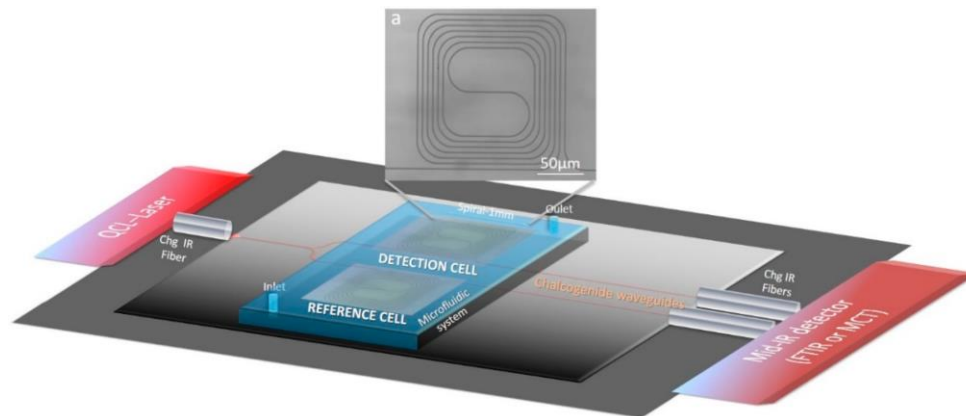


**Figure 17.** Mid-infrared (MIR) sensor scheme with an MIR source, detector, microfluidic system, and sensor fabricated from polyisobutylene (PIB) functionalized Ge-Sb-Se waveguides.

For the mid-infrared spectrum, quantum cascade lasers can be used as light sources owing to their broad emission wavelength range and high-power efficiency [92]. Regarding the optical platform, which is crucial to the sensor, although other MIR platforms such as silicon, germanium, and gallium arsenide have been investigated [83], chalcogenides have attracted much attention in the field of sensing because of their wide transparent windows in the infrared range.

Studies have reported losses in mid-infrared integrated chalcogenide devices [93,94] and high-quality factor microcavities [95,96], which can detect *E. coli* proteins in the reflection or transmission mode [97]. In 2017, Baudet et al. [98] reported that on a chalcogenide mid-infrared platform, an evanescent wave was used for mid-infrared spectroscopy analysis. The cladding layer was designed as a  $\text{Ge}_{28.1}\text{Sb}_{6.3}\text{Se}_{65}$  using magnetron sputtering, an ICP dry etching process, and a mid-infrared sensor with a guide layer of  $\text{Ge}_{12.5}\text{Sb}_{25}\text{Se}_{62.5}$ . The measured waveguide loss is approximately  $2.5 \text{ dB cm}^{-1}$  in the  $7.7 \mu\text{m}$  band.

ChG is particularly suitable for the fabrication of integrated MIR optical sensors owing to its wide transparent window and low processing temperatures. Wang et al. [99] proposed a suspended trough waveguide gas sensor for chalcogenide glass compounds that can achieve a power confinement factor greater than 90%. When the target gas was methane, the power-limiting factor of the proposed waveguide sensor was 93.81% at a wavelength of 3.67  $\mu\text{m}$ . The sensitivity was 0.4578 and the *LOD* was 18.17 ppm. When the working wavelength was 3.291  $\mu\text{m}$ , the power limiting factor was 91.98%, the sensitivity was 7.151, and the *LOD* was 1.139 ppm.

Previously, a Ge-Sb-Se chalcogenide ridge waveguide sensor with a PCF of 5% was proposed for the detection of  $\text{CH}_4$  and  $\text{N}_2\text{O}$  at 7.7  $\mu\text{m}$  [100]. In 2017, Ge-Sb-Se chalcogenide glass ridge waveguide sensors with 8% PCF were used to detect  $\text{CH}_4$  at 3.31  $\mu\text{m}$  and 7.66  $\mu\text{m}$  and  $\text{CO}_2$  at 4.3  $\mu\text{m}$  [101]. Later, Kumari proposed a silicon horizontal double-slot ridge waveguide sensor with 65.4% PCF for the detection of  $\text{CH}_4$  at 3.67  $\mu\text{m}$  [102]. In ref. [103], a ChG/silica sensor on a suspended silicon groove waveguide with a PCF of 85.77% was used to detect  $\text{CH}_4$  at 3.291  $\mu\text{m}$ . In 2020, a ChG/ $\text{SiO}_2$  sensor was implemented on a fluorine horizontal trough waveguide runway resonator with a PCF of 44.63% to detect  $\text{CH}_4$  at 3.291  $\mu\text{m}$  [44].

Chalcogenide glasses exhibit high transmission in the near- and mid-infrared regions, and good properties are obtained in thin films. Zamboni et al. [104] designed a photochemical sensor based on an anti-resonant reflective optical waveguide (ARROW) structure, as shown in Figure 18, the MZI is composed of an input waveguide and divided into two parallel arms 1 and 2, which can detect gaseous pollutants, and its characteristic vibrational absorption band is located in the mid-infrared region. In this study,  $\text{Ge}_{33}\text{As}_{12}\text{Se}_{55}$  and  $\text{Ge}_{28}\text{Sb}_{12}\text{Se}_{60}$  materials were selected. At 1.064  $\mu\text{m}$ , their bulk refractive indices are approximately 2.586 and 2.707, respectively, their transparent windows are wide (0.8–16  $\mu\text{m}$  and 1–14  $\mu\text{m}$ , respectively), and they exhibit good thermal stability. Using the 1.55  $\mu\text{m}$  waveguide, the total optical loss on the tested sample was 6 dB.

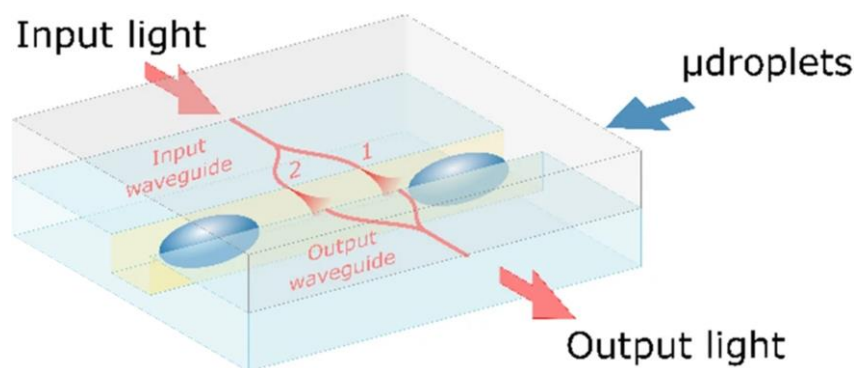


**Figure 18.** Sensing device with microfluidic circuit and MZI.

### 3.2.3. Lithium Niobate Compound MZI Optical Waveguide Sensor

Similar to SOI, LNOI has a high refractive index contrast, which strongly confines light in the micro/nano level photonic structure. From the manufacturing and application perspectives of photonic devices, it can be shown that LNOI has a transparent window in the range of visible and mid-infrared wavelengths, which makes LNOI waveguides suitable for biochemical photonics and nonlinear optical applications. Lithium niobate is transparent in the visible and mid-infrared wavelength ranges, which makes LNOI waveguides suitable for biochemical photonics [53].

Waveguide-based integrated evanescent field sensors enable the interaction between evanescent waves and the surrounding matter to detect the concentration of chemical or biochemical analytes.

Zamboni et al. [105] proposed an optofluidic device realized in monolithic lithium niobate by combining an optical waveguide with a microfluidic channel. The channel was

realized via thermal diffusion of thin strips of titanium on LN. In addition, the microfluidic channels were mechanically engraved on the same substrate using a self-polishing saw. The proposed optofluidic device was used for pH optical sensing of the analyte solutions. The detection limit was  $1.58 \pm 0.01 \mu\text{M}$ . The results showed an almost 18-fold improvement compared with polymer waveguide systems. As the Ti:LN waveguide can guide light beams of different wavelengths, the sensor can be used with pH indicators other than bromothymol blue, which increases the pH range and broadens the application range of the device. Furthermore, this device provides real-time monitoring required for a feedback system. By integrating the device with a flow controller, a solution with the desired pH can be easily obtained.

Kim et al. [106] proposed a single-mode porous silicon-integrated MZI waveguide sensor. Using the MZI-structure optical waveguide biochemical sensor to quantify the detection of isopropanol, it was shown that the exposed area would produce a large measurable phase shift of  $9.7\pi$ . The measured sensitivity of the device was as high as  $13,000 \text{ rad/RIU cm}$ , and it can detect refractive index changes as small as  $10^{-5}$ . The integrated interferometer exhibited a more stable response than the fiber-based sensing approach.

#### 3.2.4. Polymer-Based MZI Type Optical Waveguide Sensor

The refractive index of the polymer material can be adjusted, and the loss of the optical waveguide device is smaller than that of the fiber coupling. Furthermore, its preparation temperature and cost are low [107]. Therefore, polymer materials are widely used in optical waveguide devices [108,109].

Xia et al. [110] proposed polymer-based integrated optical interferometric sensors fabricated by hot-embossing and printing to realize low-cost sensors that are suitable for mass production. Polymer materials are increasingly important in the field of optical sensors owing to their diversity and compositional flexibility, as well as their ability to construct polymers using large-area printing techniques. However, special consideration must be given to polymer-based waveguide losses. In this study, an all-polymer MZI-type waveguide structure based on an inverted-ridge waveguide was proposed. The structure used a printing technique to form an inverted-ridge-groove waveguide structure in a polymethyl methacrylate (PMMA) foil. The refractive index of the core layer was in the range of 1.550–1.569. The sensor waveguide operates in a single mode, which enhances the sensitivity of the MZI sensing area to changes in the environmental refractive index and reduces the lower bending loss in the S-shaped curved waveguide.

Lab-on-a-chip technology is widely used in integrated and miniaturized chemical and biological analyses. Integrated microfluidic platforms are highly portable, and the most common microfluidic devices are based on polymer substrates such as polydimethylsiloxane (PDMS), cycloolefin copolymer (COC), and PMMA. This is because they are affordable and guarantee a high degree of flexibility in design and manufacturing.

At present, air pollution is increasingly becoming a concern, it is of great significance to develop gas sensors for volatile organic compounds (VOC) to detect polluted gases in the air. Zheng et al. [111] proposed a non-equal-width MZI optical waveguide gas sensor. By adjusting the evanescent field strength and group refractive index of the two arms of the interferometer, a refractive index sensing sensitivity of  $11,624 \text{ nm/RIU}$ , and wavelength change of  $6.8 \text{ nm}$  in the  $2.3 \text{ ppm}$  nitrobenzene gas environment were obtained through the testing of p-nitrobenzene explosive gas.

Xueke [107] designed and fabricated a biochemical sensor based on an MZI using Si/SiO<sub>2</sub> as the substrate, and the waveguide core and upper cladding were spin-coated with  $4\text{-}\mu\text{m}$  wide ZPU46 and  $9\text{-}\mu\text{m}$  wide ZPU44 polymers, respectively. The prepared polymer MZI sensor waveguide core layer size was  $4 \mu\text{m} \times 4 \mu\text{m}$ , and the bending radius and sensing window length of the Y-shaped branch structure were designed to be  $3000 \mu\text{m}$  and  $111 \mu\text{m}$ , respectively; thus, both sides of the sensing arm core layer were exposed to the solution under test, improving the sensitivity of the sensor. The refractive index ranges of

1.33–1.44 had good linearity. The average refractive index sensitivity was approximately 88 dBm/RIU, measured with glycerol aqueous solution at a wavelength of 1550 nm.

Yang et al. [112] added 5% dye material Disperse Red 1 (DR1) into a dilutive solution of SU8 photoresist and prepared DR1/SU8 polymer material for the waveguide. The structure was designed as an inverted ridge, reducing the waveguide loss of the sensor. The refractive index measured by the NaCl solution at 1550 nm wavelength is in the range of 1.585–1.593, which is significantly improved compared with that of SU8.

Yuanda et al. [5] proposed that the distance between the two arms of the MZI sensor and the length of the arms should be 400  $\mu\text{m}$  and 12,000  $\mu\text{m}$ , respectively. Because the sensitivity of the MZI sensor affects the change in the effective refractive index, the change in the effective refractive index of the sensor is in the range of 0.5–2.0 ( $\times 10^7$ ), and the corresponding output optical power change can reach the order of  $10^{-4}$ . Consequently, the MZI sensing platform has significantly high sensitivity and is suitable for applications in biochemical sensing.

Yu et al. [113] selected polymer materials for the waveguide core and upper cladding, resulting in improved sensing performance and economical and efficient mass production. When the polymer is dry-etched, the upper cladding in the sensing window is removed with ease, and the rectangular sensing arm can be approached by the analyte to form a three-dimensional (3D) structure. This structure significantly expands the sensing area and increases the sensitivity by 3.5 times. In addition, by studying the dry-etching parameters, the hydrophilicity of the polymer surface was increased, which enhanced the interaction between the guided light and the test solution. The MZI waveguide sensor proposed in this study uses the SU8 polymer as the core layer, polymethyl methacrylate-glycidyl methacrylate (PMMAGMA) as the upper cladding, and silica as the lower cladding. The refractive index measurement range at a wavelength of 1550 nm was 1.31–1.42, and the sensitivity was 225.4 dB/RIU. By optimizing the structure of the sensing arm and performing a surface treatment, the obtained sensing response time can be less than 20 s. This sensor has many advantages, such as high sensitivity and fast linear response, which are suitable for refractive index biochemical sensing.

Yu [114] proposed an asymmetric MZI sensor that designed the straight waveguide part of a Y-shaped branch as a curved structure. When the length difference between the two branches is 19.8  $\mu\text{m}$ , the refractive index is in the range of 1.470–1.545, thus maximizing the internal sensing sensitivity. The device was then fabricated using photolithography and wet etching, and the encapsulation process was optimized using PMMA films. The output power of the device was tested with benzaldehyde and ethanol mutual solutions with different refractive indices. The actual sensitivity value was 791 dB/RIU, and the sensor resolution was  $1.26 \times 10^{-6}$  RIU. Theoretically, two polymer sensor structures of symmetrical MZI and asymmetrical MZI were optimized, and the theoretical value of the sensing sensitivity increased to 1200 dB/RIU.

### 3.2.5. Gallium Arsenide-Based MZI Optical Waveguide Sensor

Gallium arsenide (GaAs) has a wide transparent window (0.9–17  $\mu\text{m}$ ) compared to Si, SiO<sub>2</sub>, polymers, and Ge, making it suitable for various electronic and optoelectronic devices. GaAs is heat-resistant, radiation-resistant, and sensitive to magnetic fields. In particular, GaAs has been considered a promising material for MIR optical devices because of its high nonlinear sensitivity, low absorption, high laser damage threshold, high thermal conductivity, and developed material technology. Wang et al. [115] proposed a mid-infrared biochemical sensor based on an asymmetric MZI with double-suspended GaAs waveguides. The design uses a suspended GaAs waveguide to enhance the interaction between the evanescent field and measured material. The asymmetric MZI structure improved the RI sensitivity of the sensor. After optimization, the NaCl solution value with different concentrations could reach 854.5 nm/RIU, whereas the value of  $Q$  obtained was 208.2.

To study a simple, low-cost, and mass-production-compatible biochemical sensor, the MZI structure was used because of its advantage of a single-signal output. Owing to the



small step in the refractive index of the polymer system between the waveguide core and cladding, the mode confinement in the polymer waveguide is small; hence, the bending radius must be large to reduce the loss and the distance between the two interference arms. Therefore, an asymmetric design of the MZI was chosen, using waveguides of different widths in the straight sections of the two interferometer arms.

Compared with inorganic material systems, polymer sensors are less sensitive owing to their low refractive index difference. Hofmann et al. [116] proposed an MZI optical waveguide refractive index sensor integrated with polymer foil. In this study, deionized water and glucose solutions were used as analytes for sensing and detecting, and the *LOD* was determined to be  $3 \times 10^{-3}$ .

Table 3 shows the performance comparison of MZI optical waveguide sensors.

**Table 3.** Performance comparison of MZI optical waveguide sensors.

Year	Unit	Construction	S (nm/RIU)	LOD (RIU)	Q
2014	Saint Petersburg Polytechnic University [73]	Single-mode silicon waveguide double transverse mode helical structure	461.6	$2.2 \times 10^{-5}$	/
2013	Bari Polytechnic University [74]	Vernier effect/Vernier effect enhanced by SOI material MZI	1000/2500 um/RIU	$10^{-7}/10^{-8}$	/
2014	Tsinghua University [75]	Large cross-section SOI ridge waveguide MZI	7396.6 %/RIU	$2.74 \times 10^{-6}$	/
2020	Zhejiang University [76]	SOI material MZI	$10^6$	$10^{-6}$	/
2014	Zhejiang University [77]	Venier effect MZI ring sensor	21,500		/
2022	University of Electronic Science and Technology of China [78]	CMOS compatible Si <sub>3</sub> N <sub>4</sub> waveguide MZI	30,000	476 ppb	/
2021	Ningbo University [99]	Chalcogenide glass compound suspension tank waveguide	7151	1.139 ppm	/
2013	University of Maryland [106]	Single-mode porous silicon integrated MZI	13,000 rad/RIU·cm	$10^{-5}$	/
2015	Southeast University [107]	Polymer MZI sensor	88 dB/mRIU	/	/
2021	University of Electronic Science and Technology [111]	Polymer-based non-monospaced MZI	11,624	/	/
2017	Jilin University [114]	PMMA film asymmetric MZI sensor	791 dB/RIU	/	/
2022	Henan Normal University [115]	Asymmetric MZI double suspended GaAs waveguide Sensor	854.5	/	208.2

"/" means that the data is not given in the reference.

### 3.3. Cascaded Structured Optical Waveguide Refractive Index Sensors

#### 3.3.1. MZI Coupled Microring Structure

Jiang et al. [117] proposed a novel high-sensitivity biosensor based on a cascaded MZI and ring resonator with a wavelength-interrogated Venier effect. Using wavelength interrogation, sensors based on MZI only and cascaded MZI rings with the Vernier effect can achieve sensitivities of 1960 nm/RIU and 19,100 nm/RIU, respectively. With the free spectral range of 600 nm, the sensitivity can be as high as 60,000 nm/RIU. A SiN sensor



chip composed of an MZI and an array waveguide grating spectrometer was realized with a detection limit of  $0.6 \times 10^{-5}$  RIU.

Linghua et al. [118] proposed a new low-cost optical waveguide polymer material, polysiloxane photonic polymer material (PSQ-Ls), and applied it to biochemical sensing of the refractive index. By introducing an MZI-type tunable coupler into the passive MRR, optical characteristic tuning under lower power consumption and three different coupling states are realized. Through experiments, it was found that UV soft imprinting technology has good compatibility with PSQ-Ls materials, and the process is simple and can be repeated. The  $Q$  values of the device in air and water can reach  $5 \times 10^4$  and  $2.7 \times 10^4$ , respectively, and the obtained absorption loss is 50 dB/cm.

### 3.3.2. Double Microring Cascade Structure

To achieve high-performance sensing devices, devices with multiple coupled or cascaded ring resonators are typically designed using two coupled rings, with the circumference of the second ring being 1–2 times that of the first ring. Compared with the structure, the fineness is enhanced, and the  $Q$  value can be  $3 \times 10^4$  or higher.

Zhu et al. proposed a high-sensitivity sensor based on a cascaded reflective MZI and MRRs [119]. As shown in Figure 19a, the sensor is composed of a microring and cascaded MZI. In Figure 19b, the microring chip was fabricated on an SOI platform. The thickness of the surface silicon layer here was 220 nm, and the thickness of the buried oxide was 2  $\mu\text{m}$ . Embedded in the trench, the sensing chip was covered with SU8 upper cladding. The microring's straight waveguide has a width of 0.5  $\mu\text{m}$ , while the ridge height, ring diameter, and ring width are 0.22, 124, and 0.5  $\mu\text{m}$ , respectively. The gap between the straight waveguide and the ring is designed to be 0.5  $\mu\text{m}$ . The reflective MZI consisted of a fiber coupler, with the two arms of the MZI coated with 200 nm Au on the output fiber ends. Compared with a traditional bipolar MRR, the sensor has an average power increase of 13 dB and can achieve a high sensitivity of 1892 dB/RIU.

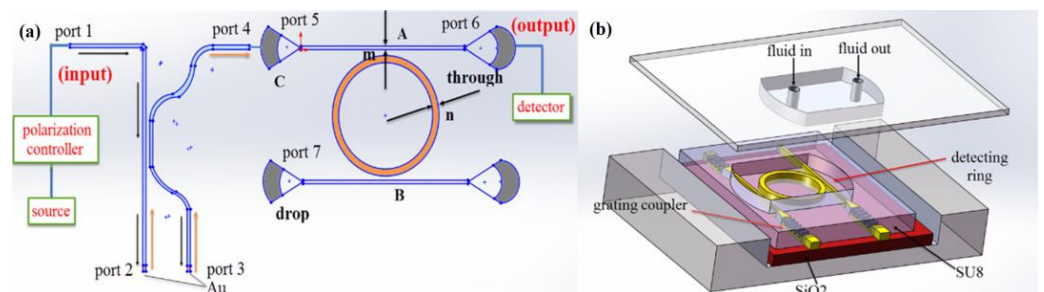


**Figure 19.** Schematic diagram of the microring and MZI cascading; (a) overall structure; (b) MRR.

Dwivedi et al. proposed a refractive index sensor utilizing the vertical coupling between two SOI waveguides [120]. A schematic diagram of the proposed sensor structure is shown in Figure 20, which consists of a planar single-mode SOI waveguide interacting with another planar single-mode SOI waveguide of length  $L$ . Thus, it consists of three planar waveguide sections: the I and III sections are identical single-mode silica-covered SOI waveguides, whereas the middle section II is a directional coupler consisting of a single-mode silica-covered SOI waveguide (WG1) and another single-mode SOI waveguide (WG2) with the covering medium as the analyte. Using optimized waveguide parameters for aqueous coverings, the bulk sensitivity of 7000 (3400) nm/RIU for a refractive index of 1.33 was achieved for TE and TM modes propagation in the optical communication band. As a result of its high bulk and thin-layer sensitivity, this sensor has potential for use in biosensing applications.

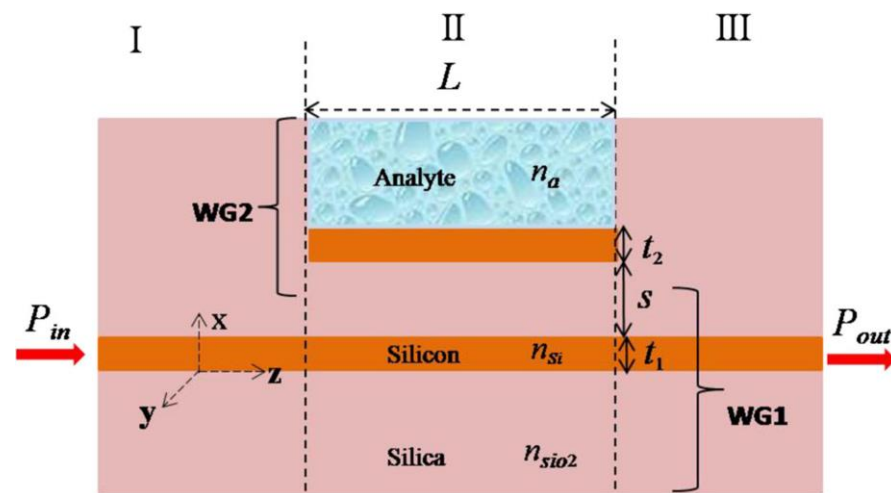


Figure 20. Schematic diagram of the refractive index sensor.

### 3.3.3. Double MZI Structure

Wei et al. [121] prepared a refractive index photopolymer microresonator sensor by direct laser writing. The sensor includes two tapered waveguides that can be directly coupled and two MZIs (“Y”-shaped waveguide of the MZI) and microcylinders transiently coupled to the MZI arms. The sensor had a sensitivity of 154.84 nm/RIU and was used to measure the refractive index of liquids. At approximately 1550 nm, the FSR of the device was approximately 16.69 and 16.48 nm in the air and water, respectively. The experiment obtained the highest Q factor of 6400.8 and 3902.5 in the air and water, respectively. The total loss of the sensor was approximately 15 dB. Using NaCl solution with a concentration of 0%–5% to measure the performance of the refractive index sensor, a sensitivity of 154.84 nm/RIU was obtained.

Dai et al. [122] proved an ultra-sensitive temperature sensor based on the SOI dual-MZI cascade, as shown in Figure 21. Sensor sensitivity is related to the FSR of the two-stage MZI, which is related to temperature sensitivity. When the FSR of the two-stage MZI is the same and the temperature sensitivity is different, the sensitivity of the entire sensor is significantly improved. This can be achieved by adjusting the structural parameters of the two-stage sensor. The sensitivity of the proposed sensor reaches 1753.7 pm/°C, which is higher than that of any temperature sensor based on the previously reported SOI platform, and 21.9 times higher than that of the conventional all-silicon temperature sensor.

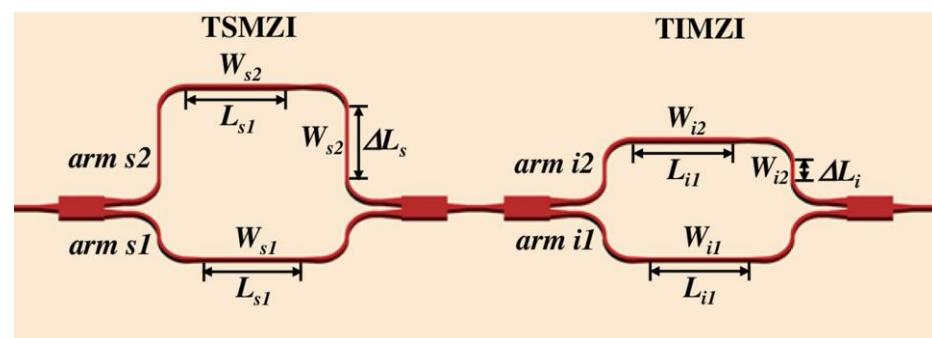


Figure 21. Schematic diagram of the sensor.

### 3.4. MMI Structured Optical Waveguide Sensor

A novel platform for chemical and biosensing based on optical MMI couplers was presented in a 2005 article by Kribich et al. [123]. A proof-of-concept humidity sensor was implemented, using hybrid sol–gel planar technology for integration onto a silicon substrate. The experiments showed that the sensor was linearly responsive to relative humidity and

the sensitivity could be adjusted using MMI design technology. Szewczuk et al. [124] also presented a waveguide sensor based on MMI in 2010. The sensor layer was used as the cover of the multimode section in the modeled systems. By selecting a material sensitive to specific external conditions as the cover of the multimode section, the sensor could be adapted to detect different physicochemical quantities. The study also investigated and compared systems based on waveguides with step index profile and gradient distribution of refractive index. It was demonstrated that the sensitivity of these systems could be adjusted by properly selecting the dimensions of the multimode section.

Copperwhite et al. [125] characterized the sensing performance of a refractometric sensing platform based on MMI couplers using a low-cost process with photocurable organic–inorganic hybrid sol–gel materials. The sensing principle is based on the sensitivity of the optical field distribution in the MMI coupler to changes in the refractive index of its environment. The length of the MMI coupler section was found to be important, with longer platforms being more sensitive. A porous sol–gel humidity-sensing enrichment layer was coated on the MMI coupler, achieving a resolution of 0.097% for relative humidity detection. The platform’s refractive index resolution was determined to be  $2 \times 10^{-6}$  RIU, making it a generic and label-free biosensor platform with immense potential for future applications.

Zinoviev et al. [126] discussed an integrated bimodal waveguide interferometric biosensor for label-free analysis, as shown in Figure 22, which was highly sensitive with a detection limit of  $2.5 \times 10^{-7}$  RIU for homogeneous sensing. It was fabricated using standard silicon technology and successfully monitored biomolecular interaction in real-time. The interferometric devices were simple and could be integrated into lab-on-a-chip platforms for point-of-care diagnostics, making them a powerful tool for biochemical analysis.

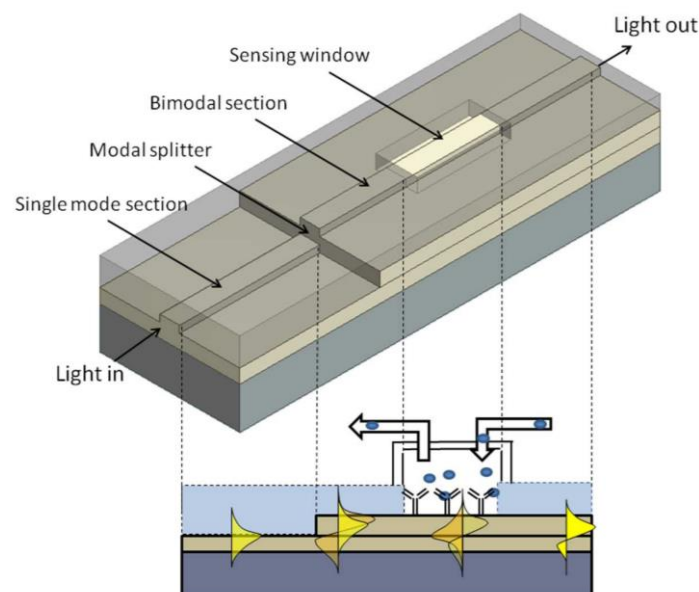


**Figure 22.** Schematic diagram of sensing waveguide structure and interaction between electromagnetic field and surface sensing molecules.

Jhonattan et al. [127] proposed and demonstrated a new evanescent wave biosensor that utilized the interaction between the fundamental and second-order modes, leading to a high sensitivity behavior. The device was designed to only allow propagation of these two modes, avoiding excitation of the first order mode, as shown in Figure 23. This design resulted in stronger interaction between the evanescent field and the outer surface compared to previous designs. The authors predicted that the limit of detection for the polymer device in bulk will be approximately  $7.34 \times 10^{-7}$  RIU.

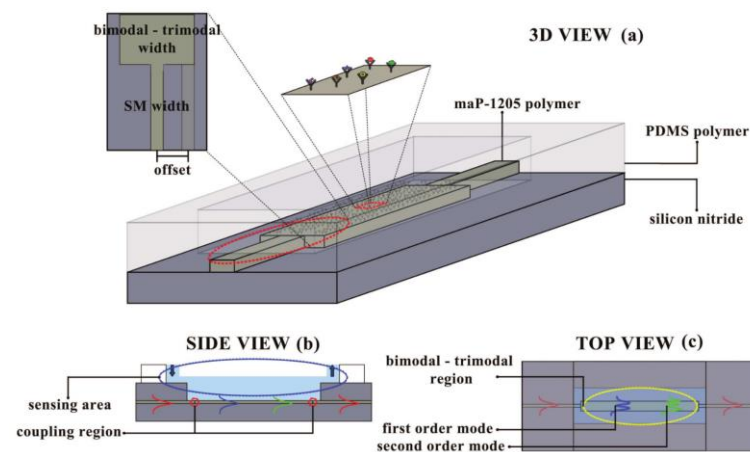


**Figure 23.** MMI biosensor scheme. (a) Three-dimensional view of the MMI and its sensing area. (b) Side view of the waveguide coupling region. (c) Top view showing the region where high-order modes are excited and interact with the bioactive region.

Kumar et al. [128] described an integrated optical waveguide refractive index sensor that had ultra-high sensitivity in the communication wavelength range. The proposed sensor can be integrated with other sensing elements on a single chip. It had a sensitivity ranging from  $\sim 1370$  to  $33,850$  nm/RIU for TM and  $1160$ – $26,050$  nm/RIU for TE polarized input light, and this is the highest sensitivity reported for MMI-based sensors. Due to the different length of the tail of TM- and TE-mode evanescent field extending out of the waveguide core, the sensitivity is different.

Ramirez et al. [129] presented an interferometric transducer that was based on a trimodal optical waveguide concept and generated a readout signal from the interference between the fundamental and second-order modes that propagated on a polymer waveguide. The device was fabricated using the polymer SU-8 over a  $\text{SiO}_2$  substrate and exhibited a free spectral range of  $20.2$  nm and signal visibility of  $5.7$  dB. The device had a high sensitivity to temperature variations of  $0.0586$  dB/ $^\circ\text{C}$ , which made it a promising candidate as a low-cost photonic transducer for use in sensing applications, including point-of-care.

The bimodal and the trimodal waveguides are both based on the interaction between the fundamental mode and the higher-order mode. Generally, the input and output waveguides are single-mode, and the middle is the interference part of multimode. When the concentration of the material to be measured changes, the effective refractive index difference between the modes changes, which changes the phase difference, and then changes the power of the fundamental mode in the output waveguide so as to achieve concentration detection.

There have been many reports on MMI fiber sensing areas in addition to the MMI planar optical waveguide sensing area. A novel leaky mode coupler of MMI fiber structure was proposed and experimentally demonstrated for surrounding refractive indices higher than that of silica fiber by Saimon et al. [130]. The proposed sensor showed a high sensitivity of  $1682$  nm/RIU and a limit of detection of  $5.94 \times 10^{-6}$  RIU, which are significantly better than those of conventional MMI waveguide sensors. In addition, ref. [131] also reviewed many other types of MMI fiber sensors and their applications, which will not be repeated in this paper.

Table 4 compares the characteristics of refractive index sensors based on three types of optical waveguide structures: MMR, MZI, and MMI, under the same conditions. Although MMR structures are widely used, their sensitivity varies greatly, with early sensitivity being relatively low. Currently, sensor schemes have achieved certain sensitivity improvements through the improvement of waveguide structures and process optimization, but the sensitivity of MMR structures is still inferior to that of MZI and MMI structures. The detection ranges of the three structure sensors do not differ significantly and all have wide detection ranges that can meet the application requirements of sensors. In terms of size,

typically, MMI sensors have smaller volumes than MMR sensors, and MMR sensors have smaller volumes than MZI sensors. In terms of processing difficulty, MMR sensors may be the most challenging to process because the diameter of the MMR is usually very small and special processing techniques are required to manufacture them. In contrast, the processing difficulty of MMI and MZI sensors may be relatively lower. In terms of losses, the losses of MZI and MMI structure sensors are relatively lower than those of MMR structures. Overall, different sensor structures may require different processing techniques and process flows, depending on factors such as materials, device size, and design requirements.

**Table 4.** Comparison of properties of three structural types.

Performance Characteristics	MRR [14,35]	MZI [72,73]	MMI [5,129]
Sensitivity (nm/RIU)	$10^2$ – $10^3$	$10^2$ – $10^4$	$10^3$ – $10^4$
Sensitivity (rad/RIU)	/	$461.6\pi$	/
Detection limit (RIU)	$10^{-2}$ – $10^{-5}$	$10^{-5}$ – $10^{-6}$	$10^{-6}$ – $10^{-7}$
Size	Smaller	Small	Smallest
Fabrication	Hard	Easy	Easy
Loss(dB/cm)	$1$ – $10^2$	<1	<1

"/" means that the data is not given in the reference.

## 4. Discussion

### 4.1. Applications in the Field of Sensing

Because optical waveguide sensors can effectively convert biological or chemical reactions into measurable signals, they are widely used in the chemical industry, biological processes, medical diagnosis, environmental monitoring, military defense, and scientific research. Optical waveguide sensors have higher sensitivity than other sensing methods [132]. Because they can be fabricated into miniaturized and integrated devices, they have been used in optical switches, sensors, and lasers [133]. Optical fibers and planar optical waveguides are common types of optical waveguides. Optical fiber sensors [134–137] have been widely used in the field of biochemical sensing; however, they are difficult to miniaturize and integrate, and biochemical modification is difficult; thus, their applications are limited. Planar optical waveguides are easy to process and modify, have high sensitivity, are easy to use, and have excellent application value in the field of biochemical sensing [138].

In terms of gas and environmental monitoring, because optical waveguide refractive index sensors have easy integration, high sensitivity, and strong anti-interference characteristics, they are widely used in the fields of toxic, flammable, and explosive gas detection, and environmental protection. The change in gas concentration can be obtained by measuring the refractive index [139]. A large number of pollutants produced by industrial production have caused serious air pollution, and the sensitive detection of volatile organic gases in the air has become a research hotspot in biochemical sensing [140].

High-precision detection technology is essential for the detection of trace biochemical compounds. Optical waveguide refractive index sensors are particularly valuable for detecting these compounds optically. They have important applications in the fields of biomedicine, human health detection, and pathogen tracing, enabling the detection of a wide range of parameters including salt concentration in water, hemoglobin concentration, glucose levels, blood pressure, E. coli, and DNA in the human body.

Chemical interactions between substances can be detected by measuring their concentrations, such as the interaction between proteins and nucleic acids or the binding of viruses and cell membrane receptors. In 2015, a simple, sensitive, and selective biosensor was proposed in the literature [141], which had a detection limit of  $1.1 \times 10^{-8}$  and a detection range of  $1 \times 10^{-8}$  to  $1 \times 10^{-6}$ . In 2018, ref. [142] described the development status of optical waveguide sensors in monitoring heavy metals, organic matter, and microbial pollution, with a detection limit of 2.2  $\mu\text{m}$  and a response time of 5 min. In 2013, a biosensor with high optical selectivity and sensitivity was proposed in ref. [143], with a detection limit of 50 CFU/mL and a detection time of 2 h. In 2020, ref. [144] studied a sensor's ability to iden-



tify mutant proteins, which had high specificity and an extremely low detection limit, with a detection limit of 11.4 fM. In 2020, ref. [145] proposed an optical biosensor that can be used for point-of-care (POC) diagnosis of 10–100 virus detection within 30 min. In 2019, ref. [146] proposed a biosensor that can be easily used to detect *Salmonella typhimurium* in vegetables with high sensitivity and specificity, and the detection limit can reach 10.2 µg/mL. In 2013, a label-free biosensor based on a polymer-coated optical waveguide was reported in ref. [147], which can detect *Escherichia coli* O157:H7. The sensor has a detection limit of 20 CFU/mL (Colony Forming Units/mL) and a response time of 30 min. In 2012, ref. [148] reported a portable, easy-to-use, and highly sensitive lab-on-a-chip biosensing device with an operability that has a detection limit of  $2.5 \times 10^{-6}$  RIU.

Other relevant literature review reports also show that optical waveguide refractive index sensors have been applied to the quantitative detection of specific chemicals, viruses, and bacteria with high sensitivity and specificity. The performance index is improving with a lower detection limit, shorter detection time, and higher sensitivity, making this type of sensor increasingly popular and widely used in biomedicine and food safety fields. However, the detection limit of the sensor is inversely proportional to the quality factor (Q) and the detection sensitivity (S) of the sensor. Therefore, to achieve a lower detection limit, the focus should be on improving the quality factor and detection sensitivity of the refractive index sensor.

#### 4.2. Comparison with Other Structures of Sensors

Research on biochemical sensors typically focuses on SPR [149–151] and waveguide grating-type sensors, which have high sensitivity and rapid response time; however, these sensors have inferior selectivity and anti-interference ability due to defects. Moreover, microrings [152–155] and MZI-type optical waveguide sensors [156,157] have high sensitivity and selectivity, strong anti-interference ability, small size, and a wide application range. This has good research significance [158]. It is reported that the microring optical waveguide and MZI optical waveguide sensing platform can detect the concentration of specific analytes above the ppm level; the microring optical waveguide sensor can effectively increase the evanescent field without increasing the length of the sensing waveguide. Furthermore, the interaction length between the field and analyte to be measured significantly reduces the size of the device.

##### 4.2.1. Bragg Grating Structure Biochemical Sensing

The reflection wavelength of a Bragg grating varies with the refractive index, and its effective refractive index decreases with a decrease in the fiber core radius and ambient refractive index. The sensitivity of the effective refractive index increases with the ambient refractive index. Therefore, the sensitivity of the sensor can be obtained by fitting the wavelength response to the range of the refractive index. In previous studies [159], the hydrofluoric acid solution chemical corrosion method was used to detect glycerin solution in the refractive index range of 1.33–1.43, and the refractive index sensitivity was 172 nm/RIU. In another study [160], the fiber radius was designed to be 0.5 µm, the sensitivities measured under the refractive index conditions of 1.20–1.30 and 1.33–1.43 are 477.33 nm/RIU and 856.30 nm/RIU, respectively. By optimizing the production parameters of the nanofiber grating, the linear sensitivity can reach 539.15 nm/RIU in the refractive index range of 1.348–1.397 [161]. It can be seen that the sensitivity and integration of Bragg grating refractive index sensing is not as good as that of optical waveguide refractive index sensing.

##### 4.2.2. Surface Plasmon Resonance Structural Biochemical Sensing

Surface plasmons are a type of surface electromagnetic wave caused by free electron oscillations on a metal surface, which realizes local enhancement of light and tuning of the electromagnetic field. It is an important research technology in the fields of micro/nano processing and integrated optoelectronics. SPR sensing technology has the advantages of

real-time monitoring, high response sensitivity, and elimination of labeling [162]. In the film structure waveguide SPR sensor, when the analyte refractive index is in the range of 1.43–1.479 at a wavelength of 850 nm, the measured sensitivity is 1489 dB/RIU, and the maximum power loss is 15.5 dB [163]. A tapered fiber-optic tungsten disulfide (WS<sub>2</sub>)-SPR sensor with enhanced sensitivity was proposed in a previous study [164]. Experiments were conducted by sequentially coating WS<sub>2</sub> and sputtering gold films onto the tapered optical fiber, as shown in Figure 24. The experimental results show that the refractive index sensitivity can reach 4158.171 nm/RIU, which is 125.8% higher than that of the multimode optical fiber SPR sensor, and higher than that of the multimode fiber SPR sensor. The tapered fiber-optic SPR sensor was improved by 50.1%. SPR sensors can achieve high sensitivity; however, they exhibit have poor selectivity and low anti-interference ability.

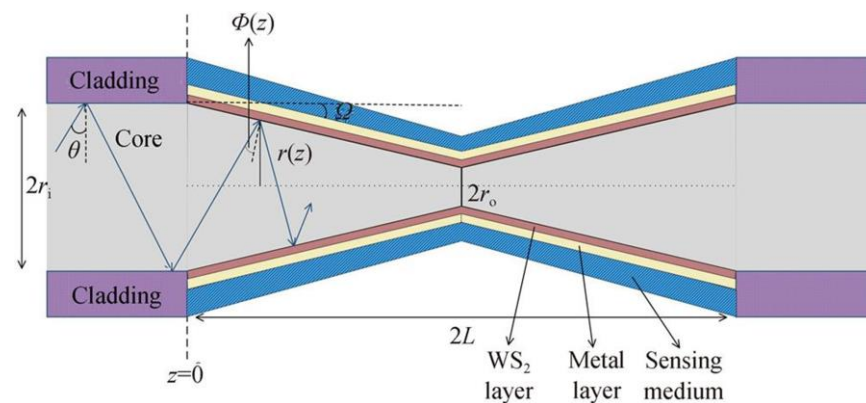


**Figure 24.** Schematic diagram of the structure of the tapered fiber optic surface plasmon resonance (SPR) sensor.

#### 4.3. Material Selection for Optical Waveguide Refractive Index Sensor

According to the previous description, the most commonly used materials for optical waveguide refractive index sensors are silicon-based materials, chalcogenide materials, lithium niobate materials, and polymer materials, as shown in Table 5.

**Table 5.** Comparing three material properties.

Refs.	Structure	Material	Sensitivity (nm/RIU)	LOD (RIU)
[37]	MRR	Si	1300	$10^{-4}$
[41]		Chalcogenide	471	$3.3 \times 10^{-4}$
[64]		LNOI	68	$10^{-2}$
[68]		Polymer	130	-
[74]	MZI	Si	$>1 \times 10^6$	$<10^{-6}$
[59,111]		Polymer	11,624	$10^{-6}$
[5,130]	MMI	Si	1682	$10^{-4}$ – $10^{-7}$
[6,130]		Polymer	-	$10^{-7}$

The sensitivity and LOD of different material systems under three sensing structures of MRR, MZI, and MMI are compared. For MRR, devices made of silicon and Chalcogenide have high sensitivity and low LOD, which are ideal materials [37,41,64,68]. For MZI, Si and polymer-based devices have similar LOD, and the former has higher sensitivity [59,74,111]. For MMI, Si-based devices have high sensitivity and LOD, polymer-based devices also have low LOD [5,6,130].

It can be seen that different materials can be selected for each refractive index sensor structure, which increases the flexibility of device design and preparation. Among them, silicon and polymer materials have a wide application range and relatively excellent performance, which can be used as the preferred material.

## 5. Summary and Outlook

### 5.1. Advantages and Disadvantages of the Sensor in Terms of Performance Indicators

It can be concluded that a perfect optical waveguide refractive index sensor would possess several key characteristics, including high sensitivity, selectivity, wide detection range, fast response, stability and repeatability, and ease of integration and automation. The ideal sensor would exhibit extremely high sensitivity, allowing for the detection of minute changes in refractive index and the ability to detect target molecules even in extremely low sample concentrations, thereby improving the accuracy and reliability of detection. To improve the selectivity and specificity of detection, the sensor should be able to distinguish between changes in the refractive index of target molecules and other molecules. A wide detection range would enable the sensor to detect target molecules in samples with different concentrations, making it suitable for a wider range of applications. The sensor should also have a fast response time to detect the presence of target molecules in a timely manner. Good stability and repeatability can ensure consistent detection performance under different environmental conditions. Finally, a perfect optical waveguide refractive index sensor should be easily integrated into practical applications and be able to automate detection operations, thereby improving detection efficiency and accuracy. Unfortunately, a perfect optical waveguide refractive index sensor is an idealized concept, and it may be challenging for an actual sensor to possess all these characteristics simultaneously. Therefore, in practical applications, it is necessary to select a suitable sensor based on specific application requirements and actual conditions and optimize and adjust its performance accordingly.

In addition, according to different application requirements, the structure of the optical waveguide refractive index sensor can be designed from the following aspects to improve device performance. First, the structure of the waveguide has an important impact on the performance of the sensor. Optimizing the size, shape, and material of the waveguide can increase the sensitivity, selectivity, and stability of the waveguide. For example, in gas detection, nanostructured waveguides can be fabricated using micro-nano fabrication techniques to improve the rate and sensitivity of gas adsorption and reaction. Second, the sensing layer is the core part of the optical waveguide refractive index sensor, and suitable sensing layer materials can be selected to achieve high sensitivity and high selectivity detection of specific chemicals, viruses, or bacteria. In gas detection, sensing layer materials with high adsorption performance can be used to increase the rate and sensitivity of gas adsorption and reaction. Third, the optimization of the optical system can improve the sensitivity, resolution, and detection range of the sensor. For example, in gas detection, light sources with multiple laser wavelengths can be used to increase the sensitivity and selectivity to different gases. Fourth, different detection methods can achieve high sensitivity and high selectivity detection of different target molecules, and the device performance can be improved by optimizing the detection method. For example, in gas detection, techniques such as surface-enhanced Raman scattering (SERS) or surface-enhanced infrared absorption (SEIRA) can be used to improve the sensitivity and selectivity of gas detection. In addition, the working environment of the sensor also has a great influence on its performance. Optimizing the working environment of the sensor can improve the sensitivity, selectivity, and stability of the sensor. For example, in gas detection, environmental factors such as the temperature and humidity of the sensor can be controlled to improve the sensitivity and selectivity of gas detection.

For instance, the microring cascading MZI structure and the double microring cascading structure discussed in this study are potential designs to consider. To enhance the sensing sensitivity of the sensor and widen the detectable range, a larger *FSR*, lower loss, high extinction ratio, and broader bandwidth are essential. Upon analyzing the loss of the optical waveguide, it becomes evident that a smaller bending radius is necessary to achieve a larger *FSR*, while a larger bending radius is required for a lower loss. Therefore, to minimize bending loss, it is necessary to optimize the confinement of the optical field with a narrower bending radius. Additionally, the performance of the sensor can be improved

by incorporating multi-ring cascading. As a result, the waveguide can be structurally engineered to achieve this goal.

It is evident that different types of optical waveguide sensors have varying performance indicators when detecting and measuring small concentrations of specific chemicals, viruses, or bacteria. These performance indicators are influenced by factors such as sensor preparation, detection substance properties, and sample processing, so it is necessary to carry out targeted design and optimization according to specific application requirements.

## 5.2. Future Direction

In recent years, with the advancement of computer and optical communication technologies, silicon photonics has rapidly developed. For silicon photonics, the most popular methods include the use of the electro-optic effect or thermo-optic effect. The use of the thermo-optic effect results in almost no additional loss, making it a preferred choice. Silicon photonics has many advantages, such as ultra-high refractive index contrast and large transparent window, and is widely used in the design, manufacture, and packaging of devices, and the sensor technology is moving towards integrated and industrial applications [165]. To obtain a highly integrated sensing system, it is necessary to integrate light sources, sensors, and detectors into one chip, and silicon photonics provide a good platform for their integration.

Photonic integration technology is a promising research field in photonics and will be significant in the field of sensing in the future. In photonic integration technology, the integration of multiple devices on multiple thin films of different materials is crucial. It is also necessary to improve chip integration and performance and reduce production costs. However, the rapid development and excellent application potential of silicon photonics have further promoted research on photonic integration [166].

MIR sensing systems that have broadband light sources can be packaged into handheld devices; however, systems based on quantum cascade lasers (QCLs) can be further scaled down to the chip level. The level of integration achievable with MIR photonic devices is expected to facilitate biomedical and diagnostic applications, as the label-free detection of biomolecular interactions, such as DNA or protein content assays, can be detected by selective MIR signatures. MIR spectroscopy is promising for the rapid screening of specific diseases of the nervous system, respiratory tract, kidney, metabolism, and genetics; however, it currently remains a research technique.

The development of technologies such as optical waveguides, silicon-based photonics, and photonic integration technology and the application of new materials have enabled the size of sensors to downscale from millimeters to microns or even nanometers, driving the trend of miniaturization and integration of sensors.

## 6. Conclusions

In this study, the basic principles of optical waveguide refractive index sensing and various design structures of refractive index sensors are introduced. The performance and development prospects of optical waveguide refractive index biochemical sensors with different structures and materials were studied by analyzing the principles and detection mechanisms of two common optical waveguide refractive index sensors.

With the rise of intelligence and informatization, the demand for biochemical sensors is constantly increasing in both biomedicine and environmental monitoring. Integrated, convenient, and accurate biochemical sensors will be the main development direction in the future. Biochemical sensors based on optical waveguide refractive index MRRs and MZI structures have the advantages of high sensitivity, high quality factor, strong anti-interference ability, easy mass production, and excellent research value. In this study, we summarized and analyzed the structural characteristics and performance indicators of two optical waveguide refractive index sensors. In particular, we compared performance indicators such as sensing sensitivity, detection range, and quality factor. The results show that the sensitivity and quality factors of the optical waveguide refractive index

sensor are mutually restricted. Compared with the microring design, the MZI sensor has higher sensitivity, whereas the MRR sensor has a higher quality factor. Optical waveguide refractive index sensors exhibit improved performance indicators; however, their structures are relatively complex.

Finally, the applications of refractive index sensing in the biochemical field for material detection are discussed. They have significant advantages over other types of biochemical optical sensors. Further research is necessary to realize sensors with high sensitivity, high quality factors, and low losses. At present, silicon photonics technology and photonics integration technology are still undeveloped; however, owing to their significant advantages, such as ultra-high refractive index contrast, wide transparent window, higher sensing sensitivity, and high integration density, they are expected to become mainstream solutions for sensing technology. Miniaturized and high-sensitivity chip sensors exhibit good prospects for development.

**Author Contributions:** Conceptualization, C.P., L.L. and H.Z.; methodology, C.P., L.L. and H.Z.; writing—original draft preparation, C.P. and H.Z.; writing—review and editing, L.L. and C.P.; visualization, C.P., C.Y. and H.T.; validation, L.L., C.Z. and L.Q.; supervision, L.L. and C.C.; project administration, L.L. All authors have read and agreed to the published version of the manuscript.

**Funding:** This work was supported by the National Key R&D Program of China (2020YFB2205902); the National Natural Science Foundation of China (62090050, 62121005, 62227819, 62274164, 62275245, 62090054); the Science and Technology Development Project of Jilin Province (202001069GX, 20200501006GX, 20200501008GX); the 17th batch of innovative and entrepreneurial talents Project in Jilin Province (2021Y008); and the Dawn Talent Training Program of CIOMP.

**Institutional Review Board Statement:** Not applicable.

**Informed Consent Statement:** Not applicable.

**Data Availability Statement:** Not applicable.

**Acknowledgments:** The authors would like to thank Jue Wang for helping with this article.

**Conflicts of Interest:** The authors declare no conflict of interest.

## References

1. Shen, L.B.; Xu, Q.B.; Jian, M.M.; Xu, J.; Dong, J.F. Development of Planar Waveguides for Optical Sensing. *Laser Optoelectron. Prog.* **2009**, *5*, 24–30. [[CrossRef](#)]
2. Cheng, J.J.; Xie, K. Progress of Waveguide Biochemical Sensors. *Laser Optoelectron. Prog.* **2005**, *11*, 17–21.
3. Lai, W.-C.; Chakravarty, S.; Wang, X.; Lin, C.; Chen, R.T. On-chip methane sensing by near-IR absorption signatures in a photonic crystal slot waveguide. *Opt. Lett.* **2011**, *36*, 984–986. [[CrossRef](#)] [[PubMed](#)]
4. Li, M.; Yue, Y.; Zhu, H.; He, J.J. Optical waveguide sensors based on Vernier effect. In Proceedings of the 2017 IEEE 16th International Conference on Optical Communications and Networks, Wuzhen, China, 7–10 August 2017; pp. 1–3.
5. Wu, Y.D.; An, J.M.; Wang, Y.; Yin, X.J.; Zhang, J.S.; Li, J.G.; Wang, H.J.; Hu, X.W. Bio-chemical Sensing platform based on Integrated Mach-Zehnder Interferometer. In Proceedings of the 2017 IEEE 13th National Optical Fiber Communication and the 14th Integrated Optics Academic Conference, Nanjing, China, 7–10 November 2017; pp. 282–285.
6. Gavela, A.F.; García, D.G.; Ramirez, J.C.; Lechuga, L.M. Last Advances in Silicon-Based Optical Biosensors. *Sensors* **2016**, *16*, 285. [[CrossRef](#)]
7. Ranacher, C.; Consani, C.; Tortschanoff, A.; Jannesari, R.; Bergmeister, M.; Grille, T.; Jakoby, B. Mid-infrared absorption gas sensing using a silicon strip waveguide. *Sens. Actuators A Phys.* **2018**, *277*, 117–123. [[CrossRef](#)]
8. Su, J. Label-Free Biological and Chemical Sensing Using Whispering Gallery Mode Optical Resonators: Past, Present, and Future. *Sensors* **2017**, *17*, 540. [[CrossRef](#)] [[PubMed](#)]
9. Fan, X.; White, I.M.; Shopova, S.I.; Zhu, H.; Suter, J.D.; Sun, Y. Sensitive optical biosensors for unlabeled targets: A review. *Anal. Chim. Acta* **2008**, *620*, 8–26. [[CrossRef](#)] [[PubMed](#)]
10. Kozma, P.; Kehl, F.; Ehrentreich-Förster, E.; Stamm, C.; Bier, F.F. Integrated planar optical waveguide interferometer bio-sensors: A comparative review. *Biosens. Bioelectron.* **2014**, *58*, 287–307. [[CrossRef](#)]
11. Patel, P. (Bio)sensors for measurement of analytes implicated in food safety: A review. *TrAC Trends Anal. Chem.* **2002**, *21*, 96–115. [[CrossRef](#)]
12. Wang, W. A review of optical waveguide biosensor especially in diamond waveguide. In Proceedings of the 2020 IEEE International Conference on Artificial Intelligence and Electromechanical Automation, Tianjin, China, 26–28 June 2020; pp. 189–192.



13. Butt, M.A.; Voronkov, G.S.; Grakhova, E.P.; Kutluyarov, R.V.; Kazanskiy, N.L.; Khonina, S.N. Environmental Monitoring: A Comprehensive Review on Optical Waveguide and Fiber-Based Sensors. *Biosensors* **2022**, *12*, 1038. [\[CrossRef\]](#)
14. Singh, A.K.; Mittal, S.; Das, M.; Saharia, A.; Tiwari, M. Optical biosensors: A decade in review. *Alex. Eng. J.* **2023**, *67*, 673–691. [\[CrossRef\]](#)
15. Yariv, A. Coupled-mode theory for guided-wave optics. *IEEE J. Quantum Electron.* **1973**, *9*, 919–933. [\[CrossRef\]](#)
16. Serval, G.; Deschacht, D. On-chip crosstalk evaluation between adjacent interconnections. In Proceedings of the 2000 IEEE 7th International Conference on Electronics, Circuits and Systems, Wuhan, China, 17–20 December 2000; pp. 827–834.
17. Dutta, A.; Deka, B.; Sahu, P.P. *Planar Waveguide Optical Sensors*; Springer International Publishing: Cham, Switzerland, 2016.
18. Elosua, C.; Bariain, C.; Matias, I.R.; Rodriguez, A.; Colacio, E.; Salinas-Castillo, A.; Segura-Carretero, A.; Fernandez-Gutiérrez, A. Pyridine Vapors Detection by an Optical Fibre Sensor. *Sensors* **2008**, *8*, 847–859. [\[CrossRef\]](#)
19. Tong, X.C. *Advanced Materials for Integrated Optical Waveguides*; Springer International Publishing: New York, NY, USA, 2014; p. 46. [\[CrossRef\]](#)
20. Soldano, L.; Pennings, E. Optical multi-mode interference devices based on self-imaging: Principles and applications. *J. Light. Technol.* **1995**, *13*, 615–627. [\[CrossRef\]](#)
21. Agrawal, N.; Zhang, B.; Saha, C.; Kumar, C.; Kaushik, B.K.; Kumar, S. Development of dopamine sensor using silver nano-particles and PEG-functionalized tapered optical fiber structure. *IEEE Trans. Biomed. Eng.* **2019**, *67*, 1542–1547. [\[CrossRef\]](#) [\[PubMed\]](#)
22. Qavi, A.J.; Kindt, J.T.; Gleeson, M.A.; Bailey, R.C. Anti-DNA: RNA Antibodies and Silicon Photonic Microring Resonators: Increased Sensitivity for Multiplexed microRNA Detection. *Anal. Chem.* **2011**, *83*, 5949–5956. [\[CrossRef\]](#) [\[PubMed\]](#)
23. De Vos, K.; Bartolozzi, I.; Schacht, E.; Bienstman, P.; Baets, R. Silicon-on-Insulator micro-ring resonator for sensitive and label-free biosensing. *Opt. Express* **2007**, *15*, 7610–7615. [\[CrossRef\]](#)
24. Hu, S.; Qin, K.; Kravchenko, I.I.; Retterer, S.T.; Weiss, S.M. Suspended micro-ring resonator for enhanced biomolecule detection sensitivity. In *Frontiers in Biological Detection: From Nanosensors to Systems VI*; SPIE: Bellingham, WA, USA, 2014; Volume 8933, pp. 33–39.
25. Robinson, J.T.; Chen, L.; Lipson, M. On-chip gas detection in silicon optical microcavities. *Opt. Express* **2008**, *16*, 4296–4301. [\[CrossRef\]](#) [\[PubMed\]](#)
26. Du, Y.; Dong, Y. The Structure Design and Simulation of the Ring Resonator Based on SOI Planar Optical Waveguide for the Micro Biochemical Sensor. *Key Eng. Mater.* **2014**, *609*, 914–920. [\[CrossRef\]](#)
27. Claes, T.; Molera, J.G.; De Vos, K.; Schacht, E.; Baets, R.; Bienstman, P. Label-Free Biosensing with a Slot-Waveguide-Based Ring Resonator in Silicon on Insulator. *IEEE Photonics J.* **2009**, *1*, 197–204. [\[CrossRef\]](#)
28. Yang, Y. Photonic Crystal Waveguide and Microcavity Controlling Light Properties and Sensing Application Research. Master's Thesis, Beijing University of Posts and Telecommunications, Beijing, China, 2018.
29. Dwivedi, R.; Kumar, A.; Tripathi, S.M. Ultra High Sensitive Refractive Index Sensor Using a Metal Under-Clad Ridge Waveguide Modal Interferometer Near the Dispersion Turning Point. *IEEE Sens. J.* **2020**, *21*, 4674–4681. [\[CrossRef\]](#)
30. Vivien, L.; Marris-Morini, D.; Griol, A.; Gylfason, K.; Hill, D.; Alvarez, J.; Sohlström, H.; Hurtado, J.; Bouville, D.; Cassan, E. Vertical multiple-slot waveguide ring resonators in silicon nitride. *Opt. Express* **2008**, *16*, 17237–17242. [\[CrossRef\]](#)
31. Zhang, X.; Guo, F.; Zhang, W.; Li, X.; Zhang, X.; Jin, H.; Jian, J.; Jin, Q. An Ag-assisted silicon slot waveguide sensor model for mid-infrared spectra gas detection with micro-ring air pressure compensation. *Optik* **2020**, *208*, 164298. [\[CrossRef\]](#)
32. Song, J.; Wang, L.; Jin, L.; Xia, X.; Kou, Q.; Bouchoule, S.; He, J.-J. Intensity-Interrogated Sensor Based on Cascaded Fabry–Perot Laser and Microring Resonator. *J. Light. Technol.* **2012**, *30*, 2901–2906. [\[CrossRef\]](#)
33. Chandran, S.; Gupta, R.K.; Das, B.K. Dispersion Enhanced Critically Coupled Ring Resonator for Wide Range Refractive Index Sensing. *IEEE J. Sel. Top. Quantum Electron.* **2016**, *23*, 424–432. [\[CrossRef\]](#)
34. Luan, E.; Yun, H.; Laplatine, L.; Dattner, Y.; Ratner, D.M.; Cheung, K.C.; Chrostowski, L. Enhanced sensitivity of subwave-length multibox waveguide microring resonator label-free biosensors. *IEEE J. Sel. Top. Quantum Electron.* **2018**, *25*, 7300211.
35. Heideman, R.G.; Lambeck, P.V. Remote opto-chemical sensing with extreme sensitivity: Design, fabrication and performance of a pigtailed integrated optical phase-modulated Mach–Zehnder interferometer system. *Sens. Actuators B Chem.* **1999**, *61*, 100–127. [\[CrossRef\]](#)
36. Prieto, F.; Sepulveda, B.; Calle, A.; Llobera, A.; Dominguez, C.; Lechuga, L. Integrated Mach–Zehnder interferometer based on ARROW structures for biosensor applications. *Sens. Actuators B Chem.* **2003**, *92*, 151–158. [\[CrossRef\]](#)
37. Zhang, W.; Serna, S.; Le Roux, X.; Vivien, L.; Cassan, E. Highly sensitive refractive index sensing by fast detuning the critical coupling condition of slot waveguide ring resonators. *Opt. Lett.* **2016**, *41*, 532–535. [\[CrossRef\]](#) [\[PubMed\]](#)
38. Huang, L.; Yan, H.; Xu, X.; Chakravarty, S.; Tang, N.; Tian, H.; Chen, R.T. Improving the detection limit for on-chip photonic sensors based on subwavelength grating racetrack resonators. *Opt. Express* **2017**, *25*, 10527–10535. [\[CrossRef\]](#)
39. Pi, M.; Zheng, C.; Peng, Z.; Zhao, H.; Lang, J.; Liang, L.; Zhang, Y.; Wang, Y.; Tittel, F.K. Theoretical study of microcavity-enhanced absorption spectroscopy for mid-infrared methane detection using a chalcogenide/silica-on-fluoride horizontal slot-waveguide racetrack resonator. *Opt. Express* **2020**, *28*, 21432. [\[CrossRef\]](#) [\[PubMed\]](#)
40. Huang, W.; Luo, Y.; Zhang, W.; Li, C.; Li, L.; Yang, Z.; Xu, P. High-sensitivity refractive index sensor based on Ge–Sb–Se chalcogenide microring resonator. *Infrared Phys. Technol.* **2021**, *116*, 103792. [\[CrossRef\]](#)
41. Zhang, X.; Zhou, C.; Luo, Y.; Yang, Z.; Zhang, W.; Li, L.; Xu, P.; Zhang, P.; Xu, T. High Q-factor, ultrasensitivity slot microring resonator sensor based on chalcogenide glasses. *Opt. Express* **2022**, *30*, 3866. [\[CrossRef\]](#)

42. Ashok, N.; Lee, Y.L.; Shin, W. GeAsSe chalcogenide slot optical waveguide ring resonator for refractive index sensing. In Proceedings of the 2017 IEEE 25th Optical Fiber Sensors Conference, Jeju Island, Republic of Korea, 24–28 April 2017; pp. 1–4. [[CrossRef](#)]
43. Richardson, K.; Petit, L.; Carlie, N.; Zdyrko, B.; Luzinov, I.; Hu, J.; Agarwal, A.; Kimerling, L.; Anderson, T. Progress on the Fabrication of On-Chip, Integrated Chalcogenide Glass (Chg)-Based Sensors. *J. Nonlinear Opt. Phys. Mater.* **2010**, *19*, 75–99. [[CrossRef](#)]
44. Wang, C.; Search, C.P. A Nonlinear Microresonator Refractive Index Sensor. *J. Light. Technol.* **2015**, *33*, 4360–4366. [[CrossRef](#)]
45. Wang, J.; Bo, F.; Wan, S.; Li, W.; Gao, F.; Li, J.; Zhang, G.; Xu, J. High-Q lithium niobate microdisk resonators on a chip for efficient electro-optic modulation. *Opt. Express* **2015**, *23*, 23072–23078. [[CrossRef](#)]
46. Wang, C.; Burek, M.J.; Lin, Z.; Atikian, H.A.; Venkataraman, V.; Huang, I.-C.; Stark, P.; Lončar, M. Integrated high quality factor lithium niobate microdisk resonators. *Opt. Express* **2014**, *22*, 30924–30933. [[CrossRef](#)]
47. Liang, H.; Luo, R.; He, Y.; Jiang, H.; Lin, Q. High-quality lithium niobate photonic crystal nanocavities. *Optica* **2017**, *4*, 1251–1258. [[CrossRef](#)]
48. Xu, M.; He, M.; Zhang, H.; Jian, J.; Pan, Y.; Liu, X.; Chen, L.; Meng, X.; Chen, H.; Li, Z.; et al. High-performance coherent optical modulators based on thin-film lithium niobate platform. *Nat. Commun.* **2020**, *11*, 3911. [[CrossRef](#)]
49. Mercante, A.J.; Shi, S.; Yao, P.; Xie, L.; Weikle, R.M.; Prather, D.W. Thin film lithium niobate electro-optic modulator with terahertz operating bandwidth. *Opt. Express* **2018**, *26*, 14810–14816. [[CrossRef](#)] [[PubMed](#)]
50. Mercante, A.J.; Yao, P.; Shi, S.; Schneider, G.; Murakowski, J.; Prather, D.W. 110 GHz CMOS compatible thin film LiNbO<sub>3</sub> modulator on silicon. *Opt. Express* **2016**, *24*, 15590–15595. [[CrossRef](#)] [[PubMed](#)]
51. Boes, A.; Corcoran, B.; Chang, L.; Bowers, J.; Mitchell, A. Status and Potential of Lithium Niobate on Insulator (LNOI) for Photonic Integrated Circuits. *Laser Photonics Rev.* **2018**, *12*, 1700256. [[CrossRef](#)]
52. Poberaj, G.; Hu, H.; Sohler, W.; Günter, P. Lithium niobate on insulator (LNOI) for micro-photonic devices. *Laser Photonics Rev.* **2012**, *6*, 488–503. [[CrossRef](#)]
53. Wang, T.-J.; Chu, C.-H.; Lin, C.-Y. Electro-optically tunable microring resonators on lithium niobate. *Opt. Lett.* **2007**, *32*, 2777–2779. [[CrossRef](#)] [[PubMed](#)]
54. Jin, M.; Chen, J.-Y.; Sua, Y.M.; Huang, Y.-P. High-extinction electro-optic modulation on lithium niobate thin film. *Opt. Lett.* **2019**, *44*, 1265–1268. [[CrossRef](#)]
55. Rao, A.; Patil, A.; Rabiei, P.; Honardoost, A.; DeSalvo, R.; Paoletta, A.; Fathpour, S. High-performance and linear thin-film lithium niobate Mach-Zehnder modulators on silicon up to 50 GHz. *Opt. Lett.* **2016**, *41*, 5700–5703. [[CrossRef](#)]
56. Mahmoud, M.; Cai, L.; Bottenfield, C.; Piazza, G. Lithium Niobate Electro-Optic Racetrack Modulator Etched in Y-Cut LNOI Platform. *IEEE Photonics J.* **2018**, *10*, 6600410. [[CrossRef](#)]
57. Lin, J.; Bo, F.; Cheng, Y.; Xu, J. Advances in on-chip photonic devices based on lithium niobate on insulator. *Photonics Res.* **2020**, *8*, 1910. [[CrossRef](#)]
58. Guarino, A.; Poberaj, G.; Rezzonico, D.; Degl'Innocenti, R.; Günter, P. Electro-optically tunable microring resonators in lithium niobate. *Nat. Photonics* **2007**, *1*, 407–410. [[CrossRef](#)]
59. Hu, H.; Yang, J.; Gui, L.; Sohler, W. Lithium niobate-on-insulator (LNOI): Status and perspectives. In *Silicon Photonics and Photonic Integrated Circuits III*; SPIE: Bellingham, WA, USA, 2012; Volume 8431, pp. 268–275.
60. Zhang, J.; Fang, Z.; Lin, J.; Zhou, J.; Wang, M.; Wu, R.; Gao, R.; Cheng, Y. Fabrication of Crystalline Microresonators of High Quality Factors with a Controllable Wedge Angle on Lithium Niobate on Insulator. *Nanomaterials* **2019**, *9*, 1218. [[CrossRef](#)]
61. Zhou, J.-X.; Gao, R.-H.; Lin, J.; Wang, M.; Chu, W.; Li, W.-B.; Yin, D.-F.; Deng, L.; Fang, Z.-W.; Zhang, J.-H.; et al. Electro-Optically Switchable Optical True Delay Lines of Meter-Scale Lengths Fabricated on Lithium Niobate on Insulator Using Photolithography Assisted Chemo-Mechanical Etching. *Chin. Phys. Lett.* **2020**, *37*, 084201. [[CrossRef](#)]
62. Wu, R.; Wang, M.; Xu, J.; Qi, J.; Chu, W.; Fang, Z.; Zhang, J.; Zhou, J.; Qiao, L.; Chai, Z.; et al. Long Low-Loss-Litium Niobate on Insulator Waveguides with Sub-Nanometer Surface Roughness. *Nanomaterials* **2018**, *8*, 910. [[CrossRef](#)] [[PubMed](#)]
63. Zhang, M.; Wang, C.; Cheng, R.; Shams-Ansari, A.; Lončar, M. Monolithic ultra-high-Q lithium niobate microring resonator. *Optica* **2017**, *4*, 1536–1537. [[CrossRef](#)]
64. Naznin, S.; Sher, M.S.M. Design of a lithium niobate-on-insulator-based optical microring resonator for biosensing applications. *Opt. Eng.* **2016**, *55*, 087108. [[CrossRef](#)]
65. Chauvet, M.; Al Fares, L.; Guichardaz, B.; Devaux, F.; Ballandras, S. Integrated optofluidic index sensor based on self-trapped beams in LiNbO<sub>3</sub>. *Appl. Phys. Lett.* **2012**, *101*, 181104. [[CrossRef](#)]
66. Suárez, I.; Matesanz, R.; De Cárcer, I.A.; Pernas, P.; Jaque, F.; Blasco, R.; Lifante, G. Antibody binding on LiNbO<sub>3</sub>: Zn waveguides for biosensor applications. *Sens. Actuators B Chem.* **2005**, *107*, 88–92. [[CrossRef](#)]
67. Bhola, B.; Nosovitskiy, P.; Mahalingam, H.; Steier, W.H. Sol-Gel-Based Integrated Optical Microring Resonator Humidity Sensor. *IEEE Sens. J.* **2009**, *9*, 740–747. [[CrossRef](#)]
68. Lv, H.L.; Liang, Y.X.; Han, X.Y.; Wu, Z.L.; Gu, Y.Y.; Zhao, M.S. Simulation and Fabrication of Polymeric Slot Waveguide for Refractive Index Sensing. *Acta Photonica Sin.* **2020**, *49*, 0213001.
69. Kim, Y.-J.; Hong, S.-H.; Lee, J.-S.; Jeon, S.-J.; Choi, W.J.; Choi, Y.-W. Thermal Reflow Effect in Multi-Mode Waveguide of S-Bend Resonator with Mode Discrimination. *IEEE Photonics J.* **2022**, *14*, 6610806. [[CrossRef](#)]

70. Chen, X.; Zhang, L.; Zhou, K.; Davies, E.; Sugden, K.; Bennion, I.; Hughes, M.; Hine, A. Real-time detection of DNA interactions with long-period fiber-grating-based biosensor. *Opt. Lett.* **2007**, *32*, 2541–2543. [[CrossRef](#)]
71. Alvarado-Méndez, E.; Rojas-Laguna, R.; Andrade-Lucio, J.; Hernández-Cruz, D.; Lessard, R.; Aviña-Cervantes, J. Design and characterization of pH sensor based on sol-gel silica layer on plastic optical fiber. *Sens. Actuators B Chem.* **2005**, *106*, 518–522. [[CrossRef](#)]
72. Du, Y.; Dong, Y. Micro biochemical sensor based on SOI planar optical waveguide. In *Selected Papers from Conferences of the Photoelectronic Technology Committee of the Chinese Society of Astronautics: Optical Imaging, Remote Sensing, and Laser-Matter Interaction*; SPIE: Bellingham, WA, USA, 2014; Volume 9142, pp. 537–546.
73. Liu, Q.; Kim, K.W.; Gu, Z.; Kee, J.S.; Park, M.K. Single-channel Mach-Zehnder interferometric biochemical sensor based on two-lateral-mode spiral waveguide. *Opt. Express* **2014**, *22*, 27910–27920. [[CrossRef](#)]
74. La Notte, M.; Passaro, V.M. Ultra high sensitivity chemical photonic sensing by Mach-Zehnder interferometer enhanced Vernier-effect. *Sens. Actuators B Chem.* **2012**, *176*, 994–1007. [[CrossRef](#)]
75. Yuan, D.; Dong, Y.; Liu, Y.; Li, T. Mach-Zehnder interferometer biochemical sensor based on silicon-on-insulator rib wave-guide with large cross section. *Sensors* **2015**, *15*, 21500–21517. [[CrossRef](#)] [[PubMed](#)]
76. Xie, Y.; Zhang, M.; Dai, D. Design Rule of Mach-Zehnder Interferometer Sensors for Ultra-High Sensitivity. *Sensors* **2020**, *20*, 2640. [[CrossRef](#)] [[PubMed](#)]
77. Jiang, X.; Chen, Y.; Yu, F.; Tang, L.; Li, M.; He, J.J. High-sensitivity optical biosensor based on cascaded Mach-Zehnder interferometer and ring resonator using Vernier effect. *Opt. Lett.* **2014**, *39*, 6363–6366. [[CrossRef](#)]
78. Zhao, K.; Dong, L.; Zheng, Y.; Deng, G.; Li, Z.; Qu, S.; Wu, J. Optimization of light-analyte interaction in Si<sub>3</sub>N<sub>4</sub>/polymer hybrid waveguide for sensitive sensing of pyridine vapor with ppb-level detection limit. *Sens. Actuators B Chem.* **2023**, *377*, 133104. [[CrossRef](#)]
79. Pejčić, B.; Eadington, P.; Ross, A. Environmental Monitoring of Hydrocarbons: A Chemical Sensor Perspective. *Environ. Sci. Technol.* **2008**, *41*, 6333–6342. [[CrossRef](#)]
80. Kim, S.-S.; Young, C.; Mizaikoff, B. Miniaturized mid-infrared sensor technologies. *Anal. Bioanal. Chem.* **2007**, *390*, 231–237. [[CrossRef](#)]
81. Hänsel, A.; Heck, M.J.R. Opportunities for photonic integrated circuits in optical gas sensors. *J. Phys. Photonics* **2020**, *2*, 012002. [[CrossRef](#)]
82. Coutard, J.G.; Brun, M.; Fournier, M.; Lartigue, O.; Fedeli, F.; Maisons, G.; Fedeli, J.M.; Nicoletti, S.; Carras, M.; Duraffourg, L. Volume Fabrication of Quantum Cascade Lasers on 200 mm-CMOS pilot line. *Sci. Rep.* **2020**, *10*, 1–8. [[CrossRef](#)]
83. Sieger, M.; Mizaikoff, B. Toward on-chip mid-infrared sensors. *Anal. Chem.* **2016**, *11*, 5562–5573. [[CrossRef](#)]
84. Su, P.; Han, Z.; Kita, D.; Becla, P.; Lin, H.; Deckoff-Jones, S.; Richardson, K.; Kimerling, L.C.; Hu, J.; Agarwal, A. Monolithic on-chip mid-IR methane gas sensor with waveguide-integrated detector. *Appl. Phys. Lett.* **2019**, *114*, 051103. [[CrossRef](#)]
85. Bodiou, L.; Dumeige, Y.; Normani, S.; Louvet, G.; Němec, P.; Nazabal, V.; Charrier, J. Design of a multimode interferometer-based mid-infrared multispecies gas sensor. *IEEE Sens. J.* **2020**, *20*, 13426–13435. [[CrossRef](#)]
86. Louvet, G.; Normani, S.; Bodiou, L.; Gutwirth, J.; Lemaitre, J.; Pirasteh, P.; Doualan, J.-L.; Benardais, A.; Ledemi, Y.; Messaddeq, Y.; et al. Co-sputtered Pr<sup>3+</sup>-doped Ga-Ge-Sb-Se active waveguides for mid-infrared operation. *Opt. Express* **2020**, *28*, 22511. [[CrossRef](#)] [[PubMed](#)]
87. Han, Z.; Singh, V.; Kita, D.; Monmeyran, C.; Becla, P.; Su, P.; Li, J.; Huang, X.; Kimerling, L.C.; Hu, J.; et al. On-chip chalcogenide glass waveguide-integrated mid-infrared PbTe detectors. *Appl. Phys. Lett.* **2016**, *109*, 071111. [[CrossRef](#)]
88. Bodiou, L.; Starecki, F.; Lemaitre, J.; Nazabal, V.; Doualan, J.-L.; Baudet, E.; Chahal, R.; Gutierrez-Arroyo, A.; Dumeige, Y.; Hardy, I.; et al. Mid-infrared guided photoluminescence from integrated Pr<sup>3+</sup>-doped selenide ridge waveguides. *Opt. Mater.* **2018**, *75*, 109–115. [[CrossRef](#)]
89. Goldsmith, H.-D.K.; Ireland, M.; Ma, P.; Cvetojevic, N.; Madden, S. Improving the extinction bandwidth of MMI chalcogenide photonic chip based MIR nulling interferometers. *Opt. Express* **2017**, *25*, 16813–16824. [[CrossRef](#)]
90. Ma, P.; Choi, D.-Y.; Yu, Y.; Yang, Z.; Vu, K.; Nguyen, T.; Madden, S. High Q factor chalcogenide ring resonators for cavity-enhanced MIR spectroscopic sensing. *Opt. Express* **2015**, *23*, 19969–19979. [[CrossRef](#)]
91. Baillieux, M.; Baudet, E.; Michel, K.; Moreau, J.; Němec, P.; Boukerma, K.; Nazabal, V. Toward chalcogenide platform infrared sensor dedicated to the in situ detection of aromatic hydrocarbons in natural waters via an attenuated total reflection spectroscopy study. *Sensors* **2021**, *21*, 2449. [[CrossRef](#)]
92. Hu, J.; Gmachl, C. QCL-based sensors target health and environmental applications. *Laser Focus World* **2012**, *48*, 39–43.
93. Ma, P.; Choi, D.-Y.; Yu, Y.; Gai, X.; Yang, Z.; Debbarma, S.; Madden, S.; Luther-Davies, B. Low-loss chalcogenide waveguides for chemical sensing in the mid-infrared. *Opt. Express* **2013**, *21*, 29927–29937. [[CrossRef](#)]
94. Tsay, C.; Zha, Y.; Arnold, C.B. Solution-processed chalcogenide glass for integrated single-mode mid-infrared waveguides. *Opt. Express* **2010**, *18*, 26744–26753. [[CrossRef](#)]
95. Singh, V.K.; Lin, P.T.; Patel, N.; Lin, H.; Li, L.; Zou, Y.; Deng, F.; Ni, C.; Hu, J.; Giammarco, J.; et al. Mid-infrared materials and devices on a Si platform for optical sensing. *Sci. Technol. Adv. Mater.* **2014**, *15*, 014603. [[CrossRef](#)] [[PubMed](#)]
96. Lin, H.; Li, L.; Deng, F.; Ni, C.; Danto, S.; Musgraves, J.D.; Richardson, K.; Hu, J. Demonstration of mid-infrared waveguide photonic crystal cavities. *Opt. Lett.* **2013**, *38*, 2779–2782. [[CrossRef](#)]



97. Anne, M.L.; Keirsse, J.; Nazabal, V.; Hyodo, K.; Inoue, S.; Boussard-Pledel, C.; Bureau, B. Chalcogenide glass optical wave-guides for infrared biosensing. *Sensors* **2009**, *9*, 7398–7411. [[CrossRef](#)] [[PubMed](#)]
98. Baudet, E.; Gutierrez-Arroyo, A.; Baillieul, M.; Charrier, J.; Nèmec, P.; Bodiou, L.; Lemaitre, J.; Rinnert, E.; Michel, K.; Bureau, B.; et al. Development of an evanescent optical integrated sensor in the mid-infrared for detection of pollution in groundwater or seawater. *Adv. Device Mater.* **2017**, *3*, 23–29. [[CrossRef](#)]
99. Wang, Y.; Chen, W.; Wang, P.; Dai, S.; Li, J.; Li, Y.; Fu, Q.; Dai, T.; Yu, H.; Yang, J. Ultra-high-power-confinement-factor integrated mid-infrared gas sensor based on the suspended slot chalcogenide glass waveguide. *Sens. Actuators B Chem.* **2021**, *347*, 130466. [[CrossRef](#)]
100. Schmidchen, J.; Splett, A.; Schüppert, B.; Petermann, K.; Burbach, G. Low loss singlemode optical waveguides with large cross-section in silicon-on-insulator. *Electron. Lett.* **1991**, *27*, 1486–1488. [[CrossRef](#)]
101. Gutierrez-Arroyo, A.; Baudet, E.; Bodiou, L.; Nazabal, V.; Rinnert, E.; Michel, K.; Bureau, B.; Colas, F.; Charrier, J. Theoretical study of an evanescent optical integrated sensor for multipurpose detection of gases and liquids in the Mid-Infrared. *Sens. Actuators B Chem.* **2017**, *242*, 842–848. [[CrossRef](#)]
102. Kumari, B.; Varshney, R.; Pal, B. Design of chip scale silicon rib slot waveguide for sub-ppm detection of N<sub>2</sub>O gas at mid-IR band. *Sens. Actuators B Chem.* **2018**, *255*, 3409–3416. [[CrossRef](#)]
103. Pi, M.; Zheng, C.; Bi, R.; Zhao, H.; Liang, L.; Zhang, Y.; Tittel, F.K. Design of a mid-infrared suspended chalcogenide/silicon-on-silicon slot-waveguide spectroscopic gas sensor with enhanced light-gas interaction effect. *Sens. Actuators B Chem.* **2019**, *297*, 126732. [[CrossRef](#)]
104. Zamboni, R.; Zaltron, A.; Chauvet, M.; Sada, C. Real-time precise microfluidic droplets label-sequencing combined in a velocity detection sensor. *Sci. Rep.* **2021**, *11*, 17987. [[CrossRef](#)]
105. Zamboni, R.; Zaltron, A.; Izzo, E.; Bottaro, G.; Ferraro, D.; Sada, C. Opto-Microfluidic System for Absorbance Measurements in Lithium Niobate Device Applied to pH Measurements. *Sensors* **2020**, *20*, 5366. [[CrossRef](#)]
106. Kim, K.; Murphy, T.E. Porous silicon integrated Mach-Zehnder interferometer waveguide for biological and chemical sensing. *Opt. Express* **2013**, *21*, 19488–19497. [[CrossRef](#)] [[PubMed](#)]
107. Shen, X.K.; Qi, Z.P.; Li, L.L.; Lin, J.; Yun, B.F.; Cui, Y.P. Design and fabrication of polymer MZI refractive index sensors. *J. Optoelectron. Laser* **2015**, *26*, 457–461.
108. Kumar, A.; Clark, D.F.; Culshaw, B. Explanation of errors inherent in the effective-index method for analyzing rectangular-core waveguides. *Opt. Lett.* **1988**, *13*, 1129–1131. [[CrossRef](#)]
109. Soref, R. Silicon-based optoelectronics. *Proc. IEEE* **1993**, *81*, 1687–1706. [[CrossRef](#)]
110. Xiao, Y.; Hofmann, M.; Sherman, S.; Wang, Y.; Zappe, H. Technology for polymer-based integrated optical interferometric sensors fabricated by hot-embossing and printing. In Proceedings of the 2015 IEEE China Semiconductor Technology International Conference, Shanghai, China, 15–16 March 2015; pp. 1–3. [[CrossRef](#)]
111. Zheng, Y.B. The Study of Silicon Nitride Waveguide Biochemical Sensor Based on Functional Polymer. Master's Thesis, University of Electronic Science and Technology of China, Chengdu, China, 2021.
112. Yang, T.F. The Planar Optical Waveguide Biochemical Sensor based on Polymer Material. Master's Thesis, Jilin University, Changchun, China, 2010.
113. Liu, Y.; Xie, T.Y.; Yi, Y.J.; Zhang, D.M. All Polymer High Accuracy MZI Waveguide Sensor. *J. Jilin Univ.* **2017**, *35*, 243–248.
114. Liu, Y. Study of all Polymer Asymmetric MZI Waveguide Refractive Index Sensor. Master's Thesis, Jilin University, Changchun, China, 2017.
115. Wang, F.; Ma, S.; Ma, T.; Wang, X.; Yu, K.; Li, L. Refractive Index Sensing Performances of a Mid-Infrared Asymmetric Mzi Based on Suspended Gaas Waveguides. *Prog. Electromagn. Res.* **2022**, *111*, 173–183. [[CrossRef](#)]
116. Hofmann, M.; Xiao, Y.; Sherman, S.; Gleissner, U.; Schmidt, T.; Zappe, H. Asymmetric Mach-Zehnder interferometers without an interaction window in polymer foils for refractive index sensing. *Appl. Opt.* **2016**, *55*, 1124–1131. [[CrossRef](#)] [[PubMed](#)]
117. Jiang, X.; Tang, L.; Song, J.; Li, M.; He, J.-J. Optical waveguide biosensor based on cascaded Mach-Zehnder interferometer and ring resonator with Vernier effect. In *Frontiers in Biological Detection: From Nanosensors to Systems VII*; SPIE: Bellingham, WA, USA, 2015; Volume 9310, p. 931003. [[CrossRef](#)]
118. Wang, L.H. Fabrication Optimisation of Polymer Integrated Photonic Devices and Their Applications. Doctoral Dissertation, Dalian University of Technology, Dalian, China, 2013.
119. Zhu, H.H.; Yue, Y.H.; Wang, Y.J.; Zhang, M.; Shao, L.Y.; He, J.J.; Li, M.Y. High-sensitivity optical sensors based on cascaded reflective MZIs and microring resonators. *Opt. Express* **2017**, *25*, 28612. [[CrossRef](#)]
120. Dwivedi, R.; Kumar, A. Refractive Index Sensing Using Silicon-on-Insulator Waveguide Based Directional Coupler. *IEEE Sens. Lett.* **2018**, *2*, 5001004. [[CrossRef](#)]
121. Wei, H.; Krishnaswamy, S. Direct laser writing polymer micro-resonators for refractive index sensors. *IEEE Photonics Technol. Lett.* **2016**, *28*, 2819–2822. [[CrossRef](#)]
122. Ding, Z.; Dai, D.; Shi, Y. Ultra-sensitive silicon temperature sensor based on cascaded Mach-Zehnder interferometers. *Opt. Lett.* **2021**, *46*, 2787–2790. [[CrossRef](#)]
123. Kribich, K.R.; Copperwhite, R.; Barry, H.; Kolodziejczyk, B.; Sabattié, J.M.; O'Dwyer, K.; MacCraith, B.D. Novel chemical sensor/biosensor platform based on optical multimode interference (MMI) couplers. *Sens. Actuators B Chem.* **2005**, *1*, 188–192. [[CrossRef](#)]

124. Szewczuk, A.; Błahut, M.; Pyka, W. Model of Optical Sensor on the Base of MMI Structures. *Acta Phys. Pol. A* **2010**, *118*, 1250–1253. [[CrossRef](#)]
125. Copperwhite, R.; Oubaha, M.; Moore, J.; McDonagh, C.; MacCraith, B.D. Sensing Performance of a Refractometric Optical Sensor Platform Based on Multimode Interference Couplers. *IEEE Sens. J.* **2011**, *11*, 3269–3275. [[CrossRef](#)]
126. Zinoviev, K.E.; Gonzalez-Guerrero, A.B.; Dominguez, C.; Lechuga, L.M. Integrated Bimodal Waveguide Interferometric Biosensor for Label-Free Analysis. *J. Light. Technol.* **2011**, *29*, 1926–1930. [[CrossRef](#)]
127. Ramirez, J.C.; Lechuga, L.M.; Gabrielli, L.H.; Hernandez-Figueroa, H.E. Study of a low-cost trimodal polymer waveguide for interferometric optical biosensors. *Opt. Express* **2015**, *23*, 11985–11994. [[CrossRef](#)]
128. Kumar, M.; Kumar, A.; Dwivedi, R. Ultra high sensitive integrated optical waveguide refractive index sensor based on mul-timode interference. *Sens. Actuators B Chem.* **2016**, *222*, 556–561. [[CrossRef](#)]
129. Ramirez, J.C.; Gabrielli, L.H.; Lechuga, L.M.; Hernandez-Figueroa, H.E. Trimodal waveguide demonstration and its implementation as a high order mode interferometer for sensing application. *Sensors* **2019**, *12*, 2821. [[CrossRef](#)] [[PubMed](#)]
130. Saimon, S.M.; Noor, M.Y.M.; Azmi, A.I.; Abdullah, A.S.; Ibrahim, M.H.; Ahmad, M.H.; Salim, M.R.; Othman, A.F.; Alqazoun, F.A.H. A High Sensitivity Refractive Index Sensor Based on Leaky Mode Coupler of MMI. *IEEE Photonics Technol. Lett.* **2021**, *34*, 63–66. [[CrossRef](#)]
131. Wang, K.; Dong, X.; Kohler, M.H.; Kienle, P.; Bian, Q.; Jakobi, M.; Koch, A.W. Advances in Optical Fiber Sensors Based on Multimode Interference (MMI): A Review. *IEEE Sens. J.* **2020**, *21*, 132–142. [[CrossRef](#)]
132. Hong, J.; Choi, J.S.; Han, G.; Kang, J.K.; Kim, C.-M.; Kim, T.S.; Yoon, D.S. A Mach-Zehnder interferometer based on silicon oxides for biosensor applications. *Anal. Chim. Acta* **2006**, *573*, 97–103. [[CrossRef](#)]
133. Wang, C.C.; Liu, R.K.; Wang, T.Y.; Li, S.S.; Zhou, G.J.; Bai, Z.X.; Wang, Y.L.; Lv, Z.W. Applications of infrared semiconductor laser. *Laser J.* **2020**, *41*, 1–10.
134. Li, Y.; Yang, K.; Liu, G.; Yao, B.; Ju, Y. 1 kHz nanosecond-pulsed room temperature Fe: ZnSe laser gain-switched by a ZnGeP<sub>2</sub> optical parametric oscillator. *Chin. Opt. Lett.* **2019**, *17*, 081404. [[CrossRef](#)]
135. Rezvani, S.A.; Nomura, Y.; Fujii, T. Generation and Characterization of Mid-Infrared Supercontinuum in Bulk YAG Pumped by Femtosecond 1937 nm Pulses from a Regenerative Amplifier. *Appl. Sci.* **2019**, *9*, 3399. [[CrossRef](#)]
136. Wang, J.; Yuan, L.; Zhang, Y.; Chen, G.; Cheng, H.; Gao, Y. Generation of 320 mW at 10.20  $\mu\text{m}$  based on CdSe long-wave infrared crystal. *J. Cryst. Growth* **2018**, *491*, 16–19. [[CrossRef](#)]
137. Huang, S.; Xiao, Y.; Liu, J.; Ji, Y.; Mao, L.; Wang, W. Nd<sup>3+</sup>-doped antimony germanate glass for 1.06  $\mu\text{m}$  fiber lasers. *J. Non-Cryst. Solids* **2019**, *518*, 10–17. [[CrossRef](#)]
138. Woodward, R.I.; Majewski, M.R.; Hudson, D.D.; Jackson, S.D. Swept-wavelength mid-infrared fiber laser for real-time ammonia gas sensing. *APL Photonics* **2019**, *4*, 020801. [[CrossRef](#)]
139. Njegovec, M.; Donlagic, D. A Fiber-Optic Gas Sensor and Method for the Measurement of Refractive Index Dispersion in NIR. *Sensors* **2020**, *20*, 3717. [[CrossRef](#)]
140. Sun, L.; Rotaru, A.; Robeyns, K.; Garcia, Y. A Colorimetric Sensor for the Highly Selective, Ultra-sensitive, and Rapid Detection of Volatile Organic Compounds and Hazardous Gases. *Ind. Eng. Chem. Res.* **2021**, *60*, 8788–8798. [[CrossRef](#)]
141. Zibaii, M.I.; Latifi, H.; Asadollahi, A.; Bayat, A.H.; Haghparast, A. DNA aptamer-based fiber optic biosensor for selective and label-free detection of dopamine. In Proceedings of the 24th International Conference on Optical Fibre Sensors, Curitiba, Brazil, 28 September–2 October 2015; Volume 9634, p. 96340X. [[CrossRef](#)]
142. Wang, N.; Dai, T.; Lei, L. Optofluidic Technology for Water Quality Monitoring. *Micromachines* **2018**, *9*, 158. [[CrossRef](#)] [[PubMed](#)]
143. Choi, E.Y.; Chang, J.H.; Hong, S.W.; Kim, S.Y.; Bae, H.J.; Park, B.Y.; Oh, M.H. Rapid Detection Methods for Food-Borne Pathogens in Milk and Dairy Products using an Optical Biosensor. *J. Dairy Sci.* **2013**, *31*, 165–170.
144. Song, S.; Lee, J.U.; Kang, J.; Park, K.H.; Sim, S.J. Real-time monitoring of distinct binding kinetics of hot-spot mutant p53 protein in human cancer cells using an individual nanorod-based plasmonic biosensor. *Sens. Actuators B Chem.* **2020**, *322*, 128584. [[CrossRef](#)]
145. Maddali, H.; Miles, C.E.; Kohn, J.; O'Carroll, D.M. Optical biosensors for virus detection: Prospects for SARS-CoV-2/COVID-19. *ChemBioChem* **2021**, *22*, 1176–1189. [[CrossRef](#)]
146. Bhandari, D.; Chen, F.-C.; Bridgman, R.C. Detection of Salmonella Typhimurium in Romaine Lettuce Using a Surface Plasmon Resonance Biosensor. *Biosensors* **2019**, *9*, 94. [[CrossRef](#)]
147. Li, B.; Ju, H. Label-free optical biosensors based on a planar optical waveguide. *BioChip J.* **2013**, *7*, 295–318. [[CrossRef](#)]
148. Estevez, M.; Alvarez, M.; Lechuga, L. Integrated optical devices for lab-on-a-chip biosensing applications. *Laser Photonics Rev.* **2012**, *6*, 463–487. [[CrossRef](#)]
149. DeBackere, P.; Scheerlinck, S.; Bienstman, P.; Baets, R. Surface plasmon interferometer in silicon-on-insulator: Novel concept for an integrated biosensor. *Opt. Express* **2006**, *14*, 7063–7072. [[CrossRef](#)] [[PubMed](#)]
150. Le, K.Q.; Bienstman, P. Enhanced Sensitivity of Silicon-On-Insulator Surface Plasmon Interferometer with Additional Silicon Layer. *IEEE Photonics J.* **2011**, *3*, 538–545. [[CrossRef](#)]
151. Abbas, A.; Linman, M.J.; Cheng, Q. Sensitivity comparison of surface plasmon resonance and plasmon-waveguide resonance biosensors. *Sens. Actuators B Chem.* **2011**, *156*, 169–175. [[CrossRef](#)] [[PubMed](#)]
152. Xu, R.; Liu, S.; Sun, Q.; Lu, P.; Liu, D. Experimental Characterization of a Vernier Strain Sensor Using Cascaded Fiber Rings. *IEEE Photonics Technol. Lett.* **2012**, *24*, 2125–2128. [[CrossRef](#)]



153. Scheler, O.; Kindt, J.T.; Qavi, A.J.; Kaplinski, L.; Glynn, B.; Barry, T.; Kurg, A.; Bailey, R.C. Label-free, multiplexed detection of bacterial tmRNA using silicon photonic microring resonators. *Biosens. Bioelectron.* **2012**, *36*, 56–61. [[CrossRef](#)]
154. Luchansky, M.S.; Bailey, R.C. High-Q Optical Sensors for Chemical and Biological Analysis. *Anal. Chem.* **2012**, *84*, 793–821. [[CrossRef](#)]
155. Ramachandran, A.; Wang, S.; Clarke, J.; Ja, S.; Goad, D.; Wald, L.; Flood, E.; Knobbe, E.; Hryniewicz, J.; Chu, S.T.; et al. A universal biosensing platform based on optical micro-ring resonators. *Biosens. Bioelectron.* **2008**, *23*, 939–944. [[CrossRef](#)] [[PubMed](#)]
156. Lapsley, M.I.; Chiang, I.K.; Zheng, Y.B.; Ding, X.; Mao, X.; Huang, T.J. A single-layer, planar, optofluidic Mach–Zehnder interferometer for label-free detection. *Lab Chip* **2011**, *11*, 1795–1800. [[CrossRef](#)]
157. Hiltunen, J.; Wang, M.; Liedert, C.; Aikio, S.; Masuda, N.; Pearce, S.; Charlton, M.; Karioja, P. Layered polymer: Inorganic composite waveguides for biosensor applications. In *Biophotonics: Photonic Solutions for Better Health Care III*; SPIE: Bellingham, WA, USA, 2012; Volume 8427, p. 84270. [[CrossRef](#)]
158. Hikita, M.; Yoshimura, R.; Usui, M.; Tomaru, S.; Imamura, S. Polymeric optical waveguides for optical interconnections. *Thin Solid Films* **1998**, *331*, 303–308. [[CrossRef](#)]
159. Yun, B.F.; Chen, N.; Cui, Y.P. Refractive Index Sensing Characteristics of Fiber Bragg Grating Based on Cladding Mode. *Acta Opt. Sin.* **2006**, *26*, 1013–1015.
160. Liu, Y.G.; Che, F.L.; Jia, Z.A.; Fu, H.W.; Wang, H.L.; Shao, M. Investigation on the characteristics of micro/nanofiber Bragg grating for refractive index sensing. *Acta Phys. Sin.* **2013**, *62*, 104218.
161. Duan, W.W. Research on Microfiber Bragg Grating with Its Fabricated Technique and Refractive Index Sensing. Master's Thesis, Xi'an Shiyou University, Xi'an, China, 2017.
162. Ray, S.; Mehta, G.; Srivastava, S. Label-free detection techniques for protein microarrays: Prospects, merits and challenges. *Proteomics* **2010**, *10*, 731–748. [[CrossRef](#)] [[PubMed](#)]
163. Yang, J.H. Study on Surface Plasmon Resonance Sensor of Polymer Optical Straight Waveguide. Master's Thesis, Dalian University of Technology, Dalian, China, 2019.
164. Zhang, W.L.; Liu, K.; Jiang, J.F.; Xu, T.H.; Wang, S.; Zhang, Z.; Jing, J.Y.; Ma, J.Y.; Liu, T.G. Tungsten Disulfide Modified Tapered Fiber Optic Surface Plasmon Resonance Sensor with Enhanced Sensitivity. *Acta Photonica Sin.* **2022**, *51*, 0306002.
165. Kazanskiy, N.L.; Khonina, S.N.; Butt, M.A. Advancement in Silicon Integrated Photonics Technologies for Sensing Applications in Near-Infrared and Mid-Infrared Region: A Review. *Photonics* **2022**, *9*, 331. [[CrossRef](#)]
166. Pelucchi, E.; Fagas, G.; Aharonovich, I.; Englund, D.; Figueroa, E.; Gong, Q.; Hannes, H.; Liu, J.; Lu, C.-Y.; Matsuda, N.; et al. The potential and global outlook of integrated photonics for quantum technologies. *Nat. Rev. Phys.* **2022**, *4*, 194–208. [[CrossRef](#)]

**Disclaimer/Publisher's Note:** The statements, opinions and data contained in all publications are solely those of the individual author(s) and contributor(s) and not of MDPI and/or the editor(s). MDPI and/or the editor(s) disclaim responsibility for any injury to people or property resulting from any ideas, methods, instructions or products referred to in the content.